

A Proposal to Jefferson Lab PAC53

The Nucleon Axial-Vector Form Factor from the $p(\vec{e}, n)\nu_e$ Reaction

X. Bai, A. Camsonne, S. Covrig, P. Degtiarenko, A. Deur, C. Ghosh, O. Hansen,
W. Henry, D. Higinbotham, D. Jones, M. Jones, C. Keppel, D. Mack, D. Meekins,
B. Raydo, R. Suleiman, A. Tadepalli, B. Wojtsekhowski (spokesperson-contact), M. Ungaro
Thomas Jefferson National Accelerator Facility, Newport News, VA 23606

A. Arcuri, D.E. King, J. Napolitano (spokesperson)
Temple University, Philadelphia, PA 19122

D. Armstrong, T. Averett (spokesperson), E. Fuchey, M. Kordosky, R. Latosky, P. Vahle
William & Mary, Williamsburg, VA 23185

M. Li, W. Xiong (spokesperson), Yi Yu
Shandong University, China

J. Golak
Jagiellonian University, PL-30348 Kraków, Poland

P. Kroll
Fachbereich Physik, Universitat Wuppertal, D-42097 Wuppertal, Germany

D. Hamilton
SUPA School of Physics and Astronomy, University of Glasgow, Glasgow G12 8QQ, UK

R. Perrino (1), L. Girlanda (1,2), G. Co'(1,2)
(1) INFN Sezione di Lecce, 73100 Lecce, Italy and
(2) Università del Salento, 73100 Lecce, Italy

O. Benhar, E. Cisbani, G. Urciuoli
INFN Sezione di Roma, 00185 Roma, Italy

A. Filippi
INFN Sezione di Torino, I-10125 Torino, Italy

M. Mirazita, S. Tomassini
INFN Laboratori Nazionali di Frascati, I-00044 Frascati, Italy

A. Bianconi (1)(2), L. Venturelli (1)(2), V. Mascagna (1)(2)
(1) Università del Brescia, 25123 Brescia, Italy and
(2) INFN Sezione di Pavia, 27100 Pavia, Italy

M. Bondì (1), G. Foti (1)(2), A. Fulci (1)(2), A. Pilloni (1)(2), M. Filippini (1)(2)
(1) INFN Sezione di Catania, 95123 Catania, Italy and
(2) Università del Messina, 98166 Messina, Italy

M. Contalbrigo (1), P. Lenisa (1)(2), L.L. Pappalardo (1)(2)
(1) INFN, Sezione di Ferrara, 44100 Ferrara, Italy and
(2) Università di Ferrara, 44121 Ferrara, Italy

G. Cates, R. Lindgren, N. Liyanage, H. Nguyen, V. Nelyubin, K. Paschke
University of Virginia, Charlottesville, VA 23904

A. Kakoyan, S. Mayilyan, A. Shahinyan
AANL, 2 Alikhanian Brothers Street, 0036, Yerevan, Armenia

D. Dutta, A. Nadeeshani, E. Wrightson, B. Tamang
Mississippi State University, Mississippi State, MS 39762

M. Bukhari
Jazan University, Jazan 45142, Saudi Arabia

A.J.R. Puckett
University of Connecticut, Storrs, Connecticut 06269, USA

D. Adhikari
Virginia Polytechnic Institute and State University, Blacksburg, VA 24061

H. Szumilla-Vance
Florida International University, Miami, FL 33199

E.C. Schulte
The Grainger College of Engineering Physics, Urbana, IL 61801

G. Niculescu
James Madison University, Harrisonburg, VA 22807

W. Brooks
Universidad Técnica Federico Santa María, Chile

(Dated: May 4, 2025)

CONTENTS

I. Executive Summary	5
A. Main physics goal	5
B. The proposed measurements/observables	5
C. Specific requirements for detectors, targets, and beam	5
D. Resubmissions	5
II. Abstract	6
III. Proposal outline	7
IV. Physics Motivation	8
A. Overview	8
B. Elastic Electromagnetic Form Factors	8
C. Elastic Axial-Vector Form Factor	9
D. GPDs and EM form factors	10
E. GPDs and the Axial-Vector Form Factor	11
F. The Pseudoscalar Form Factor	11
G. Wide Angle Compton Scattering and Axial-Vector Form Factor	12
H. World data and current interpretation of Axial-Vector Form Factor	12
1. Neutrino Quasi-elastic Scattering	13
2. Neutrino scattering from deuterium and the dipole form factor ansatz	14
3. Neutrino-proton elastic scattering in the MINERvA experiment	15
4. The Axial-Vector Form Factor from pion electro-production	15
I. Lattice QCD Calculations	17
J. Dyson-Schwinger Calculation	17
K. Summary of Physics Motivation	17
V. The Concept of the Experiment	19
A. Overview	19
B. Method of the End-point Spectrum	20
C. Kinematical parameters of the proposed experiment	21
VI. Cross section and event rate of the signal and background reactions	23
A. Axial-Vector Form Factor from $p(\vec{e}, n)\nu_e$ process	23
B. Elastic e - p process	23
C. Quasi-elastic electron scattering from Al windows	23
D. Pion-neutron photo-production process	24
E. Pion-neutron photo-production from Al target windows	24
F. Neutron-proton photo-production from Al windows	25
G. Summary of the rate estimates	25
VII. Experimental Setup	26
A. Overview	26
B. Neutron Arm	27
1. Sweeper Magnet	27
2. The Time-of-Flight Detector	27
3. The Neutron Arm Calorimeter	28
C. Veto Arm	28
1. GEM tracking detectors	29
2. Veto Arm Calorimeter	30
3. “Wide Veto” Calorimeter	30
D. Target	30
E. Beam	30
VIII. Monte Carlo simulations of the experiment	31
A. Overview	31
B. FLUKA based results	31

1. Neutron Rates	31
2. Photon Rate	31
C. Geant4 based results and comparison with FLUKA	33
D. Monte Carlo simulation of the experiment in Geant4 framework	35
E. Summary of MC result on projected accuracy	38
IX. DAQ trigger logic and rates	39
A. Overview	39
B. Online Level-0, Level-1 and Level-2 triggers	39
C. Offline Analysis and Event Rate	39
X. Preparation and Plans	40
A. Timeline	40
B. Anticipated Cost of the Neutron Arm	41
C. Workforce and Collaboration	41
XI. Summary and Beam Request	42
XII. PAC52 Review of the LOI12-24-009	43
XIII. Appendices	44
A. Wide-angle Compton Scattering	44
B. Data acquisition system	47
1. VXS Crate	47
2. JLab FADC250	48
3. JLab VTP	48
4. Streaming and Filtering logic	49
5. DAQ Crate System Layout	50
6. Conclusion	50
References	51

I. EXECUTIVE SUMMARY

We propose to demonstrate a measurement of the Axial-Vector Form Factor of the nucleon, $F_A(Q^2)$, at $Q^2 = 1$ (GeV/c)² using the fully kinematically constrained reaction $p(\vec{e}, n)\nu$. We detect the recoil neutron with a high resolution Time-of-Flight detector while vetoing pion photo-production, electron-neutron quasi-elastic scattering, and proton-neutron correlated pair events using a large acceptance charged particle spectrometer. Final background subtraction exploits the 100% parity violating nature of this reaction.

A. Main physics goal

The nucleon Axial-Vector Form Factor $F_A(Q^2)$ currently has an experimental uncertainty of 30-50%, see Sec. IV, Figure 9. A more precise measurement would provide a benchmark for lattice QCD calculations [1, 2], constrain Generalized Parton Distributions [3, 4], and provide important input for the advanced analysis of modern neutrino oscillation experiments [5]. Existing measurements, however, are systematically limited because it has not yet been possible to measure the fundamental reaction with both well-defined kinematics and sufficient precision.

We propose an apparatus that will use the CEBAF polarized electron beam to obtain a statistically limited measurement of $F_A(Q^2)$ with precision higher than existing results. This is based on making the ground breaking extraction of a tiny signal under a very large background by noting that the reaction only proceeds for left-handed electrons. This demonstration will allow us to extend, in the future, the Axial-Vector Form Factor study to lower and higher Q^2 values.

B. The proposed measurements/observables

Using a polarized electron beam on a liquid hydrogen target, the cross section for the reaction $p(\vec{e}, n)\nu_e$ will be determined, see also [6, 7]. With 50 days of beam time, the Axial-Vector Form Factor can be determined at $Q^2 = 1$ (GeV/c)² with a relative accuracy of 39%, close to the goal in last year's LOI [8]. In the case of the commonly used dipole fit, $F_A = g_A/(1 + Q^2/M_A^2)^2$, the corresponding relative accuracy for M_A will be 20%.

C. Specific requirements for detectors, targets, and beam

- Neutron detection: The primary trigger will be a neutron event in the neutron detector. A time-of-flight system (TOF) will have a set 1540 counters similar to those currently used in CLAS12, capable of reaching ≤ 100 ps time resolution. The TOF system will be used to measure the time of the trigger with respect to the beam bunch time to identify neutrons from the $p(\vec{e}, n)\nu_e$ reaction. Located behind the TOF system, a highly segmented hadron calorimeter (NCAL) will provide a DAQ trigger. A sweeper magnet located near the target will allow us to reduce random low-energy background and deflect protons from the detector acceptance.
- A veto spectrometer consisting of a tracker (8 layers of GEM chambers from the Hall A SBS spectrometer) and the SBS trigger calorimeter, HCAL, to reject events coincident with the primary trigger. The primary background processes are e -n quasi-elastic scattering from the Al windows of the LH2 target, positive pion photo-production from hydrogen, and neutrons from short-range correlated proton-neutron pairs in the Al windows.
- 25-cm-long liquid hydrogen target (collimated to 10 cm by tungsten blocks).
- 120 μ A electron beam at energy 2.2 GeV with 85% longitudinal polarization and 8 ns bunch structure.

D. Resubmissions

The current proposal is based on LOI-12-24-009 from PAC52 [8]. The goal of this proposal overlaps significantly with the LOI from PAC1 [6] and LOI-04-006 from PAC25 [7].

II. ABSTRACT

The nucleon Axial-Vector Form Factor has been an important part of hadron physics since the 1960s [9] and a number of pion electro-production experiments were made [10, 11] with the goal of extracting F_A even with significant model dependence. Neutrino scattering experiments from hydrogen and deuterium bubble chambers [12] have also been performed, but the results for F_A had low accuracy due to limited statistics. A recent result from MINER ν A [5] improved the accuracy of F_A significantly, and comparison with a direct study of the $p(\bar{e}, n)\nu_e$ reaction, which we are proposing, will be useful.

The experiment will use a polarized electron beam and a liquid hydrogen target. We will detect outgoing neutrons from the charged current (CC) reaction $p(\bar{e}, n)\nu$ in a neutron arm consisting of time-of-flight detectors and a hadron calorimeter, which will allow us to determine the axial vector form factor of the nucleon at $Q^2 = 1$ (GeV/c)². Neutrons from this reaction must be separated from two large backgrounds: 1) protons from e -p elastic EM scattering and 2) neutrons from pion photo-production. Most of the elastic protons will be swept off the acceptance of the neutron detector using a 1 Tesla-meter magnet. Neutrons from pion photo-production will be eliminated using geometric and timing information from the neutron detector to precisely reconstruct the energy of the incident electron. A time resolution of 100 ps is required.

The experiment will take advantage of the high longitudinal polarization of the electron beam and 100% physics asymmetry of the CC reaction to obtain the final number of desirable neutrons. The electron beam will have energy of 2.2 GeV and current of 120 μ A for production running. Calibration of the neutron calorimeter using e -p events and rejection of backgrounds in production running will be done using a “veto” spectrometer consisting of the GEMS and HCAL.

The expected result for the Axial-Vector Form Factor will have 39% relative accuracy. Assuming a dipole form factor, the relative accuracy for M_A from the proposed data point will be 20%.

III. PROPOSAL OUTLINE

This section provides an introduction to the document. The goal of the proposed experiment is to measure the cross section of the reaction $p(\vec{e}, n)\nu$ at $Q^2 = 1$ $(\text{GeV}/c)^2$. We will detect outgoing neutrons from the reaction $p(\vec{e}, n)\nu_e$ in a neutron detector consisting of a time-of-flight detector and a hadron calorimeter. The experiment will allow us to determine the axial vector form factor of the nucleon with accuracy of 39%.

The experiment will take advantage of the high degree of longitudinal polarization of the electron beam and 100% asymmetry of the reaction to obtain the final result. The electron beam will have energy of 2.2 GeV and a current of 120 μA . Calibration of the time-of-flight and the neutron calorimeter, and further rejection of backgrounds will be done using a “veto” spectrometer consisting of the existing GEM-based chamber tracker and hadron calorimeter, HCAL.

In the development of the proposal for $p(\vec{e}, n)\nu_e$ we selected a momentum transfer for which the time-of-flight resolution of the neutron detector allows dramatic reduction of the background. The choice of $Q^2 = 1$ $(\text{GeV}/c)^2$ is also good for constraining M_A . We evaluated the intensity of the background by direct calculations based on published data. Analytic estimates are used for the development of the apparatus configuration. After that, the layout was optimized and expected accuracy was calculated by using the results from Monte Carlo simulations based on Geant4 and FLUKA.

The text of the proposal is organized as follows:

- Section I is the executive summary of the proposal.
- Section II is the abstract of the proposal.
- Section III provides the outline of the proposal.
- Section IV presents the physics motivation and formalism.
- Section V presents the concept of experiment.
- Section VI presents the cross sections and rates.
- Section VII describes the experimental layout and detectors.
- Section VIII presents the MC simulations in FLUKA and Geant4.
- Section IX outlines the logic of DAQ triggers and off-line analysis.
- Section X covers details of the timeline, construction cost, and workforce.
- Section XI presents the beam time request and expected result.
- Section XII shows the report from PAC 52 on LOI12-24-009.
- Appendix A (in section XIII) is a note written by P. Kroll on Wide-angle Compton Scattering.
- Appendix B (in section XIII) is a description of DAQ for calorimeters, time-of-flight system, and GEM chambers.

IV. PHYSICS MOTIVATION

A. Overview

Investigation of the hadron structure is a primary mission of the DOE Thomas Jefferson National Accelerator Facility (TJNAF). It is presented in the Long Range Plan formulated by DOE NSAC which can be seen here [13]. Section 9.2.4. named ‘‘Continuous Electron Beam Accelerator Facility at Jefferson Lab’’ briefly outlines the current plans for TJNAF.

The reaction under discussion, $p(\vec{e}, n)\nu_e$, is the inverse of neutron beta decay at high Q^2 . It is related to one of the classical processes of nuclear physics, whose studies led to the theory of the weak interaction about 90 years ago. The nucleon Axial-Vector Form Factor has been an important part of nucleon physics [9] and a number of pion electron-production experiments were made [10, 11] with the goal of extracting F_A even with significant model dependence. Neutrino scattering experiments from hydrogen and deuterium bubble chambers [12] were also performed but had low accuracy due to limited statistics. A recent result from MINER ν A [5] improved the accuracy of F_A significantly, but a direct study with $p(\vec{e}, n)\nu_e$ reaction will be very useful.

The study of neutrino physics is currently a major topic for the US physics community [14]. The reaction $p(\vec{e}, n)\nu_e$ is directly connected to the beta decay process, careful investigations of which are in progress in DOE labs [15]. JLab has already done experiments [16–18] motivated by the need for improved data related to neutrino-nuclei interactions.

Development of the Generalized Parton Distributions [19–21] gave a consistent formalism for the nucleon electromagnetic and weak current form factors, specifically F_A [3]. The GPD-based theory of Wide-Angle Compton Scattering [22] predicted a polarization parameter K_{LL} directly connected to the same GPDs as F_A . This prediction was confirmed by JLab experiment E99-114 [23]. Lattice QCD calculations [1, 2], as well as a calculation using the DSE method [24], have recently advanced in their predictions for the Axial-Vector Form Factor.

The CEBAF accelerator at TJNAF provides a continuous electron beam with a current up to 120 μ A and energy up to 11 GeV with a high degree of longitudinal polarization (routinely 85%). Such a beam has been used in a number of high precision experiments including the study of parity violation in electron-proton elastic scattering and double polarization electron-neutron and electron-proton scattering. The E91-017/E00-006(G0) experiment [25, 26] used the polarized beam with 32 ns bunch structure and a current of 40 μ A for the time-of-flight measurement of the recoil proton.

By now, four LOIs [6–8, 27] on the Axial-Vector Form Factor have been submitted to the JLab PACs over 37 years, but this is the first fully developed proposal. PAC52 gave a positive review of the LOI 12-24-009 (see section XII) and encouraged us to submit a full proposal.

In this section we discuss the status of the vector and axial vector nucleon form factor data and related physics.

B. Elastic Electromagnetic Form Factors

The cross section for elastic e -N scattering is given by the Rosenbluth formula below and includes the Sachs electromagnetic form factors, G_E and G_M , which are well-measured for Q^2 up to ~ 10 GeV².

$$\left. \frac{d\sigma}{d\Omega} \right|_{lab} = \left. \frac{d\sigma}{d\Omega} \right|_{Mott} \frac{E'}{E} \left(\frac{G_E^2 + \tau G_M^2}{1 + \tau} \cos^2 \frac{\theta}{2} + 2\tau G_M^2 \sin^2 \frac{\theta}{2} \right), \quad (1)$$

where $\tau = Q^2/4M^2$, E is the incident electron energy, $-Q^2$ is the four-momentum transfer squared and θ is the electron scattering angle. For reference, the Sachs form factors are related to the Dirac and Pauli form factors, F_1 and F_2 , resp., as

$$\begin{aligned} G_E &\equiv F_1 - \kappa\tau F_2 \\ G_M &\equiv F_1 + \kappa F_2, \end{aligned} \quad (2)$$

where κ is the anomalous magnetic moment. As shown in Figure 1 [28], below $Q^2 = 1 \text{ GeV}^2$, the proton form factors are well-described by the dipole form factor, $G_D(Q^2)$,

$$G_D(Q^2) = \frac{1}{(1 + Q^2/M_V^2)^2}, \quad (3)$$

where $M_V = 0.843 \text{ GeV}$ and Q^2 is measured in GeV^2 . Ignoring relativistic effects, the Fourier transform of G_D gives a spatial dipole distribution for the electric charge and magnetization.

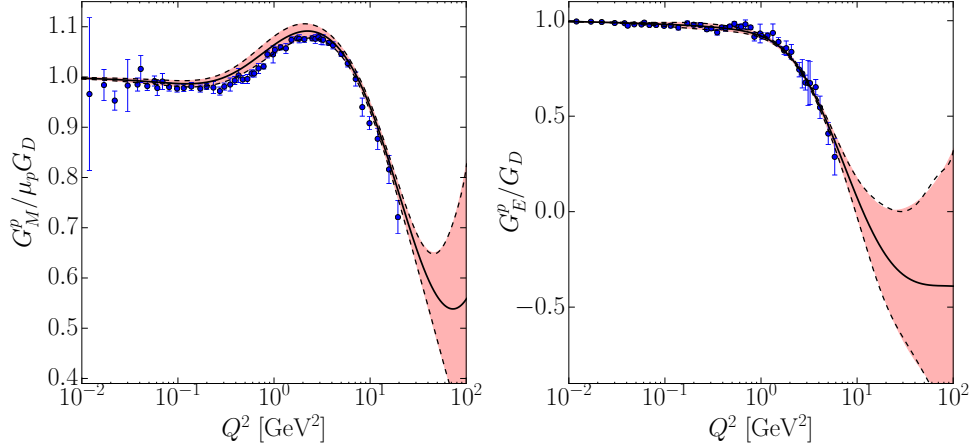


FIG. 1. This figure shows a parameterization of world data for G_M^p/G_D (left) and G_E^p/G_D (right) [28]. Both are well-described by the dipole form factor below $Q^2 = 1 \text{ GeV}^2$.

C. Elastic Axial-Vector Form Factor

In this section we present the cross section and formalism used to study the proposed $p(\vec{e}, n)\nu$ reaction shown in Figure 2. In contrast with the electromagnetic case, much less is known about the elastic axial-vector form factor, $F_A(Q^2)$, which contributes to the cross section for measurements where a charged, weakly-interacting boson is exchanged.

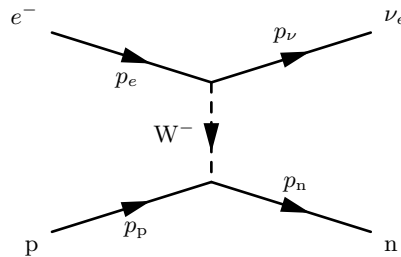


FIG. 2. The Feynman diagram of the reaction studied in this experiment, $p(\vec{e}, n)\nu_e$. The kinematics are elastic with the interaction mediated by the exchange of a W^- boson.

P. Kroll [29] recently provided the formalism and cross-section formula for the reaction presented here. We define the four-momenta of the incoming and outgoing proton and neutron as $p_i = p_p$, $p_f = p_n$, resp. We define the four-momenta of the incoming and outgoing electron and neutrino as p_e and p_ν , resp. We will ignore the masses of the leptons and define m as the nucleon mass. We assume the absence of second class currents and the validity of the Partially Conserved Axial Vector Current (PCAC) hypothesis. We define $\Delta = p_f - p_i$, and the relevant Mandelstam

variables are given below.

$$\begin{aligned}
s &= (p_i + p_e)^2 \\
&= (p_f + p_\nu)^2 \\
t &= (p_f - p_i)^2 \\
&= (p_\nu - p_e)^2
\end{aligned} \tag{4}$$

The matrix element of the hadronic weak current, $J^\mu = V^\mu(0) - A^\mu(0)$ is defined as follows:

$$\langle n(p_f) | J^{\mu\dagger}(0) | p(p_i) \rangle = \bar{u}(p_f) \left[F_1^{(3)}(t) \gamma^\mu + F_2^{(3)}(t) \frac{i\sigma^{\mu\nu} \Delta_\nu}{2m} - F_A^{(3)}(t) \gamma^\mu \gamma_5 - F_P^{(3)}(t) \frac{\gamma_5 \Delta^\mu}{2m} \right] u(p_i) \tag{5}$$

The EM isovector form factors are defined in terms of the proton and neutron Dirac and Pauli form factors as $F_i^{(3)} = F_i^p - F_i^n$, where $i = 1, 2$. The $F_A^{(3)}$ and $F_P^{(3)}$ are axial-vector, and pseudo-scalar, isovector form factors, resp.

The amplitude for the process in Figure 2 is given by the product of the lepton current and the hadron current given in equation (5),

$$M = \frac{G}{\sqrt{2}} \cos \theta_c \bar{u}_\nu(p_\nu) \gamma_\mu (1 - \gamma_5) u_e(p_e) \times [\text{Equation (5)}], \tag{6}$$

where G is the Fermi coupling constant and θ_c is the Cabibbo angle.

The cross section for unpolarized beam and target is:

$$\frac{d\sigma}{dt} = \frac{1}{2\pi} \frac{1}{(s - m^2)^2} \left(\frac{G \cos \theta_c}{\sqrt{2}} \right)^2 \times \{ \}, \tag{7}$$

where

$$\{ \} = \left\{ (s - m^2)^2 \left(F_1^{(3)2} + F_A^{(3)2} \right) \right. \tag{8}$$

$$\left. + t \left[s F_1^{(3)2} - \frac{(s - m^2)^2}{4m^2} F_2^{(3)2} + (s - 2m^2) F_A^{(3)2} \right. \right. \tag{9}$$

$$\left. - 2(s - m^2) \left(F_1^{(3)} + F_2^{(3)} \right) F_A^{(3)} \right] \tag{10}$$

$$\left. + \frac{1}{2} t^2 \left[\left| F_1^{(3)} + F_2^{(3)} - F_A^{(3)} \right|^2 - \frac{s}{2m^2} F_2^{(3)2} \right] \right\} \tag{11}$$

The contribution of $F_P^{(3)}$ to the cross section is suppressed by the ratio of the electron to nucleon mass squared, $(m_e/m)^2$ [30], and for $Q^2 = 1 \text{ GeV}^2$, it is estimated that $F_P^{(3)} \simeq F_A^{(3)}$. Thus, we can ignore the contribution from $F_P^{(3)}$.

For a beam of left-handed electrons,

$$\left(\frac{d\sigma}{dt} \right)_L = 2 \frac{d\sigma}{dt} \tag{12}$$

and for right-handed,

$$\left(\frac{d\sigma}{dt} \right)_R = 0 \tag{13}$$

D. GPDs and EM form factors

The material presented here is based on the formalism of Diehl et al. [3]. The proton and neutron Dirac and Pauli form factors may be expressed in terms of contributions from u, d and s quarks as,

$$\begin{aligned}
F_i^p &= e_u F_i^u + e_d F_i^d + e_s F_i^s, \\
F_i^n &= e_u F_i^d + e_d F_i^u + e_s F_i^s
\end{aligned} \tag{14}$$

where $i = 1, 2$ and the e_q are the charges of the quarks in units of $|e|$. Neglecting contributions from strange quarks we can obtain the u and d flavor form factors as

$$\begin{aligned} F_i^u &= 2F_i^p + F_i^n \\ F_i^d &= 2F_i^n + F_i^p \end{aligned} \quad (15)$$

Defining $H^q(x, t)$ and $E^q(x, t)$ as the proton GPDs for unpolarized quarks of flavor q at zero skewness, we can define the quantities

$$\begin{aligned} H_v^q(x, t) &= H^q(x, t) - H^{\bar{q}}(x, t) \\ E_v^q(x, t) &= E^q(x, t) - E^{\bar{q}}(x, t), \end{aligned} \quad (16)$$

where \bar{q} refers to anti-quark with flavor q . The difference between quarks and anti-quarks in equation (16) means there is no contribution from strange or sea quarks, thus the subscript v which denotes valence quarks. The flavor form factors, F_i^q , are related to these GPDs by

$$F_1^q(t) = \int_0^1 dx H_v^q(x, t), \quad F_2^q(t) = \int_0^1 dx E_v^q(x, t). \quad (17)$$

At $t = \xi = 0$ and $x > 0$, $H^q(x) = q(x)$ and $H^{\bar{q}}(x) = \bar{q}(x)$, which are the quark and anti-quark densities, resp. and thus

$$F_1^u(0) = 2, \quad F_1^d(0) = 1, \quad F_1^s(0) = 0 \quad (18)$$

For F_2 , the normalization is chosen as $F_2^q(0) = \mu_q$, thus $\mu_u = 2\mu_p + \mu_n = 1.67 \mu_N$ and $\mu_d = \mu_p + 2\mu_n = -2.03 \mu_N$, where μ_N is the nuclear magneton.

E. GPDs and the Axial-Vector Form Factor

The isovector axial vector form factor defined as, $F_A^{(3)}(t) = F_A^p(t) - F_A^n(t)$, can be written in terms of $\tilde{H}^q(x, t)$, the proton GPD for longitudinally polarized quarks. We define the valence contribution as the difference between the quark and antiquark distributions,

$$\tilde{H}_v^q(x, t) = \tilde{H}^q(x, t) - \tilde{H}^{\bar{q}}(x, t) \quad (19)$$

and write

$$F_A^{(3)}(t) = \int_0^1 dx \left[\tilde{H}_v^u(x, t) - \tilde{H}_v^d(x, t) \right] + 2 \int_0^1 dx \left[\tilde{H}^{\bar{u}}(x, t) - \tilde{H}^{\bar{d}}(x, Q^2) \right]. \quad (20)$$

Note that the second integral contains contributions from the u and d sea quarks. At $t = \xi = 0$ and $x > 0$, $\tilde{H}^q(x) = \Delta q(x)$ and $\tilde{H}^{\bar{q}}(x) = \Delta \bar{q}(x)$, where $\Delta q(x)$ and $\Delta \bar{q}(x)$ are the densities of longitudinally polarized quarks and anti-quarks, resp. Unlike H and E , which are much better constrained by the extensive dataset for $F_1(Q^2)$ and $F_2(Q^2)$, the GPD \tilde{H} is poorly constrained due to the dearth of precision data for $F_A^{(3)}(Q^2)$ and the relatively narrow range of Q^2 coverage.

F. The Pseudoscalar Form Factor

Though its contribution is relatively small and will be ignored in the cross section formalism, for completeness we show the connection between the least well-known GPD, $\tilde{E}(x, t)$, and the isovector pseudoscalar form factor, $F_P^{(3)}(t) = F_P^p(t) - F_P^n(t)$.

$$F_P^{(3)}(t) = \int_0^1 dx \left[\tilde{E}_v^u(x, t) - \tilde{E}_v^d(x, t) \right] + 2 \int_0^1 dx \left[\tilde{E}^{\bar{u}}(x, t) - \tilde{E}^{\bar{d}}(x, Q^2) \right] \quad (21)$$

G. Wide Angle Compton Scattering and Axial-Vector Form Factor

The Real Compton Scattering (RCS) process is shown in Figure 3 where a real photon scatters from a single quark while the others are spectators. While the photon can also scatter from a quark that is interacting with the rest of the nucleon through the exchange of hard gluons, it was observed that the RCS process mostly occurs through the handbag process [23, 31–33] as was predicted by A. Radyushkin [34] and P. Kroll [22]. The hard-scale physics is contained in the scattering from a single active quark and is calculable using pQCD and QED as it is simply Compton scattering from a structureless spin-1/2 particle. The soft physics is contained in the wave function describing how the active quark couples to the rest of the proton. This coupling is fully described in terms of GPDs [4], see Appendix A.

A summary of the RCS physics is given here. The cross section for Compton scattering is:

$$\frac{d\sigma}{d\Omega} = \frac{\pi\alpha^2}{(s-m^2)^2} \frac{(s-u)^2}{-us} \left[R_V^2(t) + \frac{t^2}{(s-u)^2} R_A^2(t) - \frac{t}{4m^2} R_T^2(t) \right], \quad (22)$$

where the R_i are related to moments of the zero-skewness GPDs as

$$R_{V(T)}(t) = \int_{-1}^1 \frac{dx}{x} H^a(E^a)(x, 0, t), \quad R_A(t) = \int_{-1}^1 \frac{dx}{x} \text{sign}(x) \tilde{H}^a. \quad (23)$$

The GPDs H and E have been reasonably determined by EM form factor data and thus the RCS form factors, R_V and R_T . As before, \tilde{H} is not well constrained and thus R_A is not well-constrained. Constraining \tilde{H} requires accurately measuring F_A . Using valence quark GPDs to calculate the RCS form factors gives results for the cross section that agree fairly well with data [4].

There are also two polarization observables in RCS. They are A_{LL} and K_{LL} , correlations between the helicity of the incoming photon and the helicity of incoming proton (A_{LL}) or outgoing proton (K_{LL}). These correlations are given approximately by:

$$A_{LL} = K_{LL} \simeq 2 \frac{-t}{s-u} \frac{R_A(t)}{R_V(t)}. \quad (24)$$

Thus, the measurement of these polarization observables allows us to put a constraint on R_A and the GPD \tilde{H} . See Appendix A and Ref. [4].

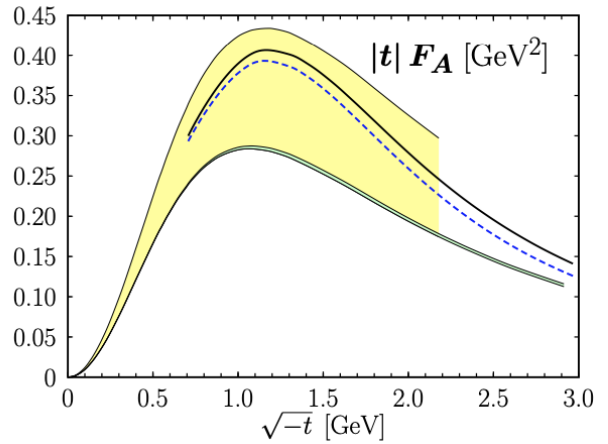
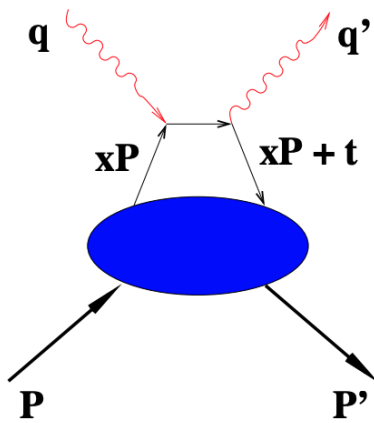


FIG. 3. The handbag diagram for RCS and plot of $|t| \times F_A$ vs. momentum transfer $\sqrt{-t}$ from Ref. [4].

H. World data and current interpretation of Axial-Vector Form Factor

In this section we review existing measurements of F_A . These measurements fall into four categories: 1) neutrino quasi-elastic scattering from a variety of heavier nuclei, from carbon to lead, using neutrino beams produced for neutrino oscillation measurements, 2) neutrino scattering from deuterium in bubble chambers, 3) a recent measurement of neutrino-proton elastic scattering from the MINER ν A experiment and 4) experiments using pion electro-production.

Neutrino oscillation experiments rely on QE neutrino scattering from a wide range of nuclei for detecting neutrinos. The relatively poor statistics of these measurements along with a variety of experimental uncertainties requires comparison of data to Monte-Carlo simulations. The simulation relies on models of QE scattering using assumptions about the free-nucleon axial vector form factor, F_A , and poorly known nuclear corrections [35].

The majority of measurements have taken place in the last several decades using beams produced for neutrino oscillation experiments. While these beams provide a relatively high neutrino flux, the energy distribution is poorly known as they are produced in secondary processes. As an example, the MINER ν A experiment at Fermilab created a neutrino beam (NuMI) in a two-step process where protons with energy 120 GeV from the main injector are incident on a carbon target producing, among other particles, pions and kaons [36].

These mesons are focused along the beam direction and eventually decay, producing a beam composed primarily of ν_μ . The flux and kinematic distribution of the beam must be simulated, see Figure 4. In Ref [37], neutrinos with a broadband energy spectrum between 2-20 GeV, peaking at 3 GeV, were scattered from C, Fe and Pb and compared to scattering from CH in the form of scintillator. The inelastic cross section ratio for lead to CH is shown in Figure 5, where it is seen to deviate significantly from the Monte Carlo prediction.

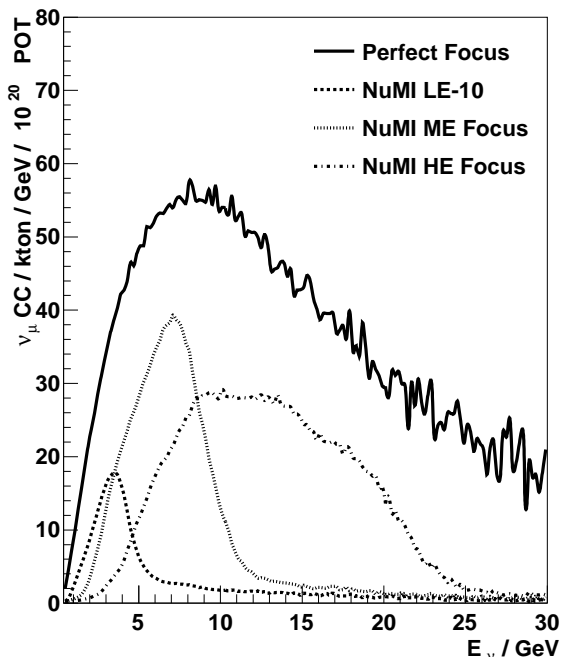


FIG. 4. This plot shows three *simulated* neutrino energy spectra from the NuMI beam for different focusing schemes. The data in Figure 5 used the so-called “LE-10 focus”, peaking at 3 GeV. The solid line shows the expected spectrum if all mesons could be focused precisely along the beam axis.

The neutrino flux is simulated using GEANT4 and the neutrino interactions in the detector are simulated using the GENIE [38] event generator, described below. The paper states that an array of nuclear models was used for the simulation, none of which is confirmed by the data. It further states that the failure of nuclear scaling models in the large x region has profound implications for neutrino oscillation experiments that utilize QE events.

GENIE is a Monte-Carlo simulation used to model neutrino interactions, in particular for interpreting neutrino events in oscillation experiments. It is pieced together from a range of models necessary to cover the broad kinematic range from perturbative to non-perturbative pictures of the nucleon. The authors state that a fundamental problem is the lack of data and that most simulations are tuned to ν -d bubble chamber data taken in the 70s and 80s. GENIE models QE scattering using the standard cross section formalism, noting that the axial-vector form factor, F_A , is the sole unknown quantity. They chose to use a dipole form factor with its one free parameter, the axial mass.

For neutrino oscillation measurements, events are detected by neutrino interactions with nuclei. It is not possible to

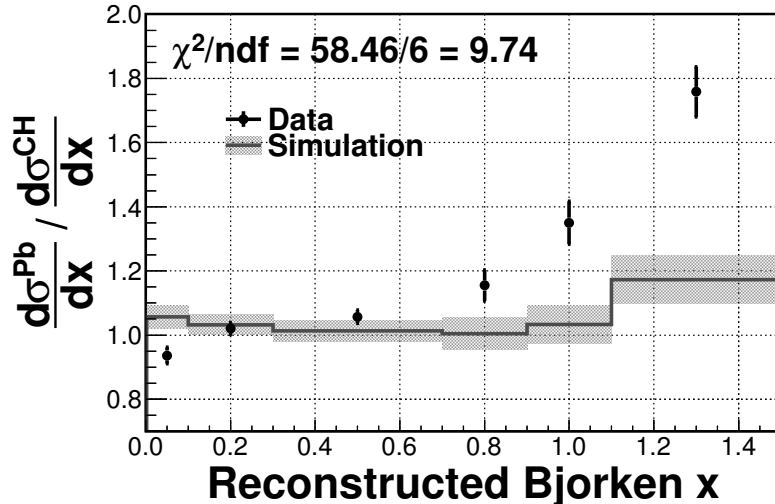


FIG. 5. This plot shows the measured ratio of the inclusive ν_μ scattering cross sections of lead to CH (plastic scintillator) versus Bjorken x . Scattering is predominantly quasielastic. Error bars on the data (simulation) show the statistical (systematic) uncertainties.

distinguish the (dominant) quasielastic from inelastic interactions using data. Simulation must be used to disentangle the spectra and it relies on the poorly known axial vector form factor. The other large uncertainty stems from a lack of knowledge of nuclear corrections and, in particular, final state interactions. Clearly, an accurate, kinematically constrained measurement of F_A to better understand the QE neutrino scattering cross sections is of substantial value to the neutrino community.

2. Neutrino scattering from deuterium and the dipole form factor ansatz

Axial vector form factor measurements from bubble chamber experiments between 1973-90 were made using quasi-elastic neutrino scattering from deuterium [12]. See Figure 6. These experiments are kinematically constrained due to the ability to track the final-state particles. Because the nucleus was deuterium, it was assumed the nuclear effects were relatively small. In analyzing the data it was also assumed the axial vector form factor could be described by a dipole form factor,

$$F_A(Q^2) = \frac{F_A(0)}{(1 + Q^2/M_A^2)^2}, \quad (25)$$

where $F_A(0) = 1.2754 \pm 0.0013$ is precisely measured in neutron beta decay, see Ref. [39], and $M_A \simeq 1.08$ (GeV/c)², the only free parameter, is the axial mass.

It is this data that has been used for decades as the best model for a free nucleon form factor. Extractions of the axial vector form factor from heavier nuclei also assume a dipole form factor but have poorly known nuclear corrections and poorly constrained kinematics. Figure 7 shows the broad range of extractions of M_A from experiment and lattice QCD [40].

More recently the so-called ‘ z -expansion’ formalism [12] has been used to provide a model-independent, QCD-based parameterization of F_A . Note that this formalism is now regularly used for fitting the EM form factors [28] as well. This method relaxes the strict shape requirement of the dipole and gives an uncertainty for F_A from the bubble chamber experiments *that is nearly an order of magnitude larger than previously assumed* [12]. This leads to a 50% uncertainty in the weak charge radius [1]. An uncertainty in the axial vector form factor that is possibly a factor of 10 larger than previously thought has profound implications for the uncertainties given in neutrino oscillation experiments.

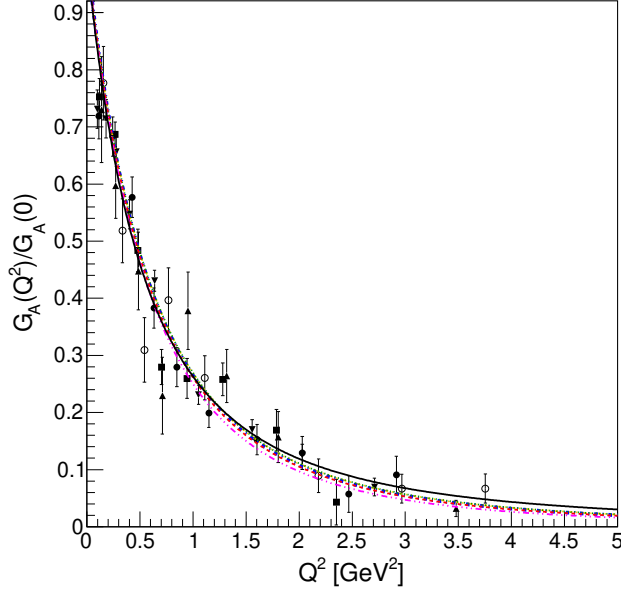


FIG. 6. Results for $G_A(Q^2)/G_A(0)$ for $\nu - d$ scattering from bubble chamber experiments. Note that these authors use the notation G_A instead of F_A for the axial vector form factor.

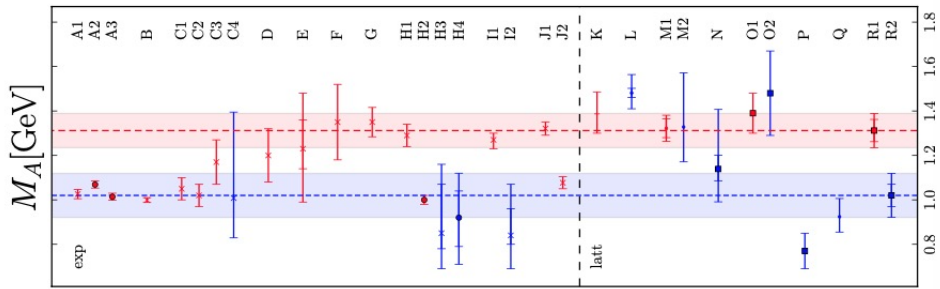


FIG. 7. This plot shows a wide range of values for the axial mass. A-J are experimental results while K-R are LQCD calculations. Points in are red are extracted assuming a dipole form factor. Points in blue are extracted by measuring the slope of F_A obtained using the z -expansion.

3. Neutrino-proton elastic scattering in the MINERvA experiment

Recently the MINERvA collaboration published the first accurate measurement of ν -proton elastic scattering from protons in CH (plastic scintillator) [5]. Their results are shown in Figures 8 and 9. Several features worth noting are the broad range of Q^2 , the modeling that must be done to extract results with a QE-like signature in the presence of many non-QE contributions, the disagreement with the model at both low and high Q^2 , and the disagreement of the data with data for a ‘free’ proton based on ν -d bubble chamber data.

4. The Axial-Vector Form Factor from pion electro-production

Pion electroproduction near threshold allows one to indirectly extract $F_A(Q^2)$ [9–11], but the numerical value is highly model-dependent and can be interpreted in different theoretical frameworks. The spread between the different approximations and sets of data is sizable and should be considered as an intrinsic systematic uncertainty in the

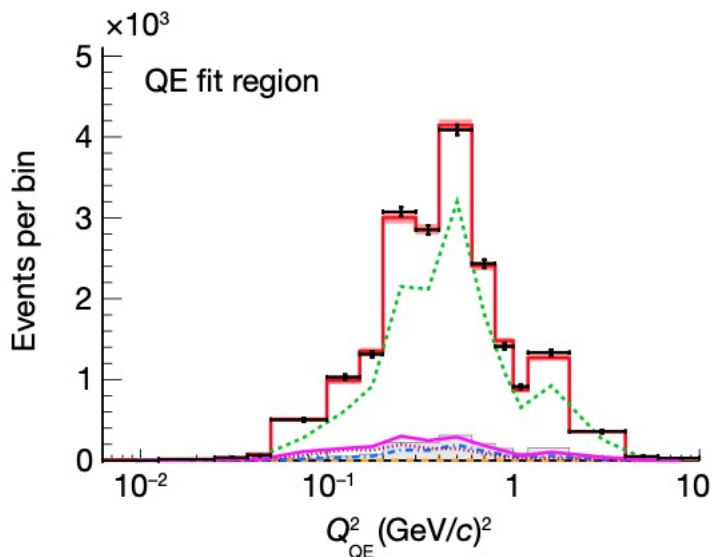


FIG. 8. This plots shows measured data (black points) from the MINERνA experiment. Note the broad range in Q^2 . The red shaded band is the prediction from Monte-Carlo simulations. The curves represent the estimated elastic contributions to the Monte-Carlo from elastic and inelastic scattering processes. The dashed green line is the estimated elastic ν -p contribution.

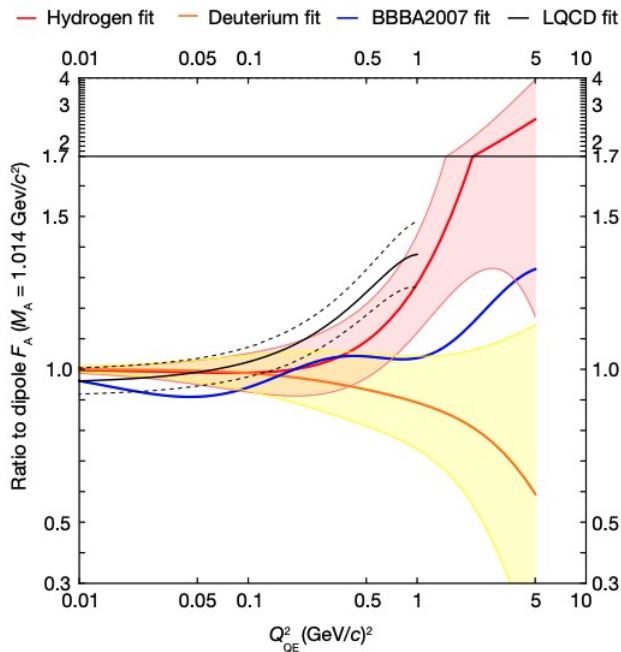


FIG. 9. This plot shows the ratios of various form factor results to the dipole form factor. The red curve is a fit to the recent MINERνA proton data; a z expansion formalism fit to deuterium (bubble chamber data) is shown in orange; blue is an empirical fit to deuterium and pion electro-production data; the black curve is a fit to recent lattice QCD calculations. Note the poor agreement of the MINERνA data with the early deuteron data and the decent agreement with LQCD calculations.

extraction of the form factor [35]. Data from this method are shown in Figure 10.

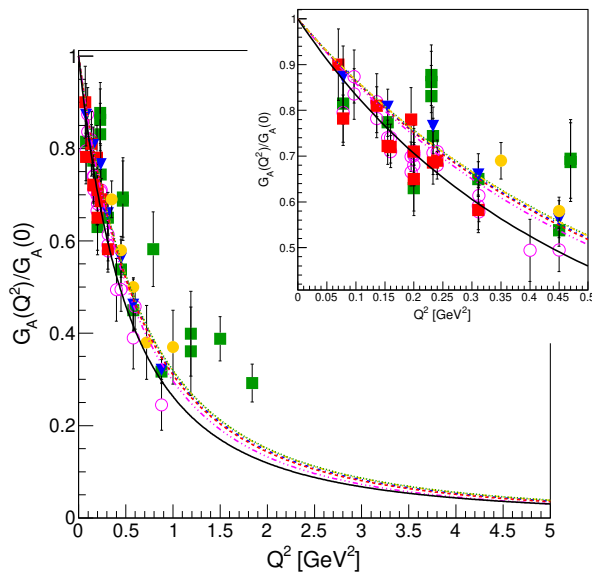


FIG. 10. Data for $G_A(Q^2)/G_A(0)$ from pion electro-production. Note that these authors use the notation G_A instead of F_A for the axial vector form factor. Figure is from Ref. [35].

I. Lattice QCD Calculations

A summary of recent lattice QCD (LQCD) work relevant to νA scattering is presented in Ref. [1]. Here we paraphrase the authors. Calculations of neutrino-nucleus cross sections begin with the neutrino-nucleon interaction, making the latter critically important to flagship neutrino oscillation experiments, despite limited measurements with poor statistics. The presence of multiple interaction channels and the addition of nuclear effects significantly complicates the analysis of data and gives rise to a major source of uncertainty. Recent LQCD results for F_A , with quantifiable theoretical uncertainties, are consistent with each other, but collectively disagree with a fit to the ν -d bubble chamber results. See Figure 11. A significant challenge toward a theoretical description of νA scattering is the lack of data with which to benchmark parts of the calculation. Given the challenge to benchmark νA QE cross section models, scientists have relied heavily on sparse data from early bubble chamber experiments on hydrogen and deuterium.

LQCD calculations are in good agreement with the precisely measured axial coupling, $g_A = F_A(0)$, with one group achieving a sub-percent agreement [1].

J. Dyson-Schwinger Calculation

Calculations presented in Ref. [24] are using a Poincaré-covariant quark+diquark Faddeev equation and related symmetry-preserving weak interaction current. It has parameter-free predictions for the nucleon axial-vector form factor, $F_A(Q^2)$, provides a detailed analysis of the flavor separation of the proton F_A into contributions from valence u and d quarks, and with available form factors, validates the predicted roles of non-pointlike quark+quark (diquark) correlations within the nucleon. The results of F_A calculations based on the Dyson-Schwinger method are shown in Fig. 12 taken from the Ref. [24].

K. Summary of Physics Motivation

Existing measurements of F_A have come from quasi-elastic reactions with neutrinos, pion electroproduction and a recent ν -p measurement by the MINER νA collaboration. Due to the nature of the neutrino beams, the kinematics of the reactions are not well-known and the statistics are poor. Results from pion electroproduction are model-dependent. While neutrino scattering from nuclei provides useful data on the nature of neutrino interactions used in large-scale neutrino detectors, extracting information on F_A for a free proton requires poorly understood nuclear corrections and final-state interactions. There are three primary physics motivations for the measurement proposed

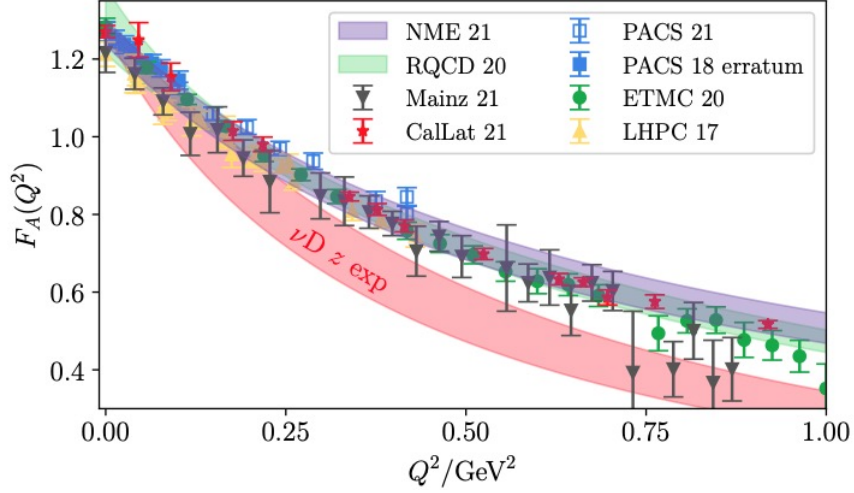


FIG. 11. The red curve shows $F_A(Q^2)$ from a fit of ν -d bubble chamber data using the z -expansion. All other curves and points are lattice calculations at the physical pion mass. Figure is from Ref. [1].

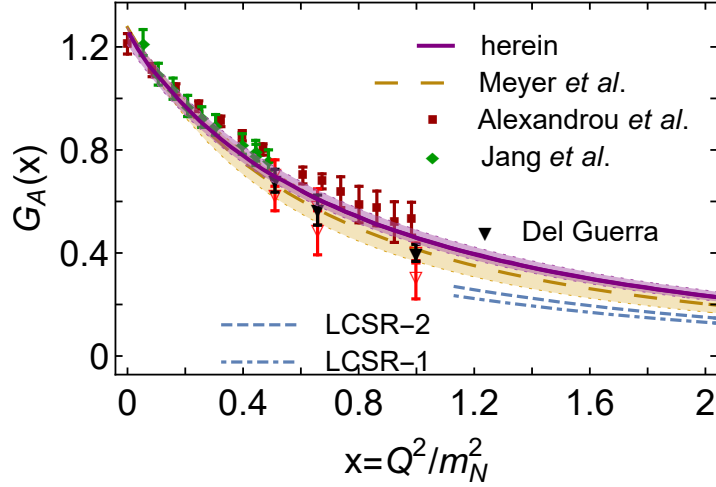


FIG. 12. Axial-Vector Form Factor data and calculations. The “herein” is the DSE result. Note that these authors use the notation G_A instead of F_A for the axial vector form factor. Figure is from Ref. [24].

here:

- 1) It is a fundamental nucleon form factor that is poorly known, including its kinematic dependence and connection to the weak nucleon structure. Lattice QCD calculations are robust but current data are unable to accurately verify the calculations.
- 2) The Axial-Vector Form Factor provides a constraint on two of the GPDs that EM form factors cannot provide.
- 3) It is of interest to the neutrino oscillation community to reduce systematic uncertainties due to the lack of a precise, kinematically constrained, measurement of F_A on a free proton.

The proposed experiment will provide a new measurement of the Axial-Vector Form Factor using the previously unused $p(\vec{e}, n)\nu_e$ reaction at $Q^2 = 1 \text{ GeV}^2$ with relative statistical accuracy 39% and systematics of 5%.

V. THE CONCEPT OF THE EXPERIMENT

A. Overview

The process we propose to study is the $p(\vec{e}, n)\nu_e$ reaction at $Q^2=1$ (GeV/c)² with the goal of achieving a 39% accuracy measurement of the Axial-Vector Form Factor. Note that the idea of making such a type of measurement at Jefferson Lab was outlined by J. Napolitano [6] in an LOI, which was submitted to JLab PAC1.

Detection of the weak charge current process (CC) is not an easy task because the total production rate at maximum JLab luminosity is on the order of a few Hz and neutrino detection is not practical (detection efficiency is 10^{-12} for a 10-ton/m² detector).

Detection of the recoil neutron is possible, but there are several processes which lead to a huge background (up to 10^7 times more intense than the CC). They are electron-proton scattering, pion photo-production when the recoil neutron has almost the same energy as in the CC, electron-neutron scattering and photo-induced neutron-proton pair production (short-range correlation process) in the target cell windows. In addition, measurement of the neutron speed based on the beam RF time deals with determination of the correct bunch, which is complicated by a large flux of slower neutrons produced by the prior bunches. The solution of the misidentified beam bunch problem is a two-component neutron arm which allows measurement of the neutron speed independently of the beam bunch information. The loss of detector efficiency due to such neutron “tracking” is a factor of two.

Several orders of reduction of the background will be achieved by using a modern, high-resolution Time-of-Flight neutron detector (TOF) and a pulsed electron beam (8 ns beam bunch structure). A combination of 100 ps time resolution, a 15-m-long path from the target to the detector, and a short 10 cm target will allow us to reconstruct the incident electron/photon energy to the level of 1%, see more in sec. VI.

Electron-proton elastic scattering events are removable by using a 1-Tesla-meter sweeper magnet with vertical field direction located between the target and the neutron detector.

The rate of neutrons from pion photo-production rapidly decreases near the elastic peak in the reconstructed beam energy spectra and is additionally suppressed by using a large acceptance veto arm for the correlated pions. Backgrounds produced in the windows of the target will be removed using a tungsten collimator and will also be suppressed by using the veto arm.

The projected signal-to-background ratio is quite small, on the order of a few 10^{-3} . A key part of the experimental concept is measuring the beam helicity correlation, R , in the detected event rates ($N_{+/-}$): $R = (N_+ - N_-)/(N_+ + N_-)$ for positive and negative helicity of the beam electrons. This parameter for the CC reaction is equal to 1, but it is very small and known for the background processes. Even with a tiny value of R , determination of the CC cross section is achievable. Projected statistics of the CC events is 9.55k, so with $R = 6.8 \times 10^{-4}$, see more in sec. VI and sec. VIII, the accuracy for the CC cross section will be on the order of 39%.

Several effects contribute to the systematical uncertainty of the cross section measurement in the case of $p(\vec{e}, n)\nu_e$. They are the beam polarization, which will be known to 2% or better, the beam intensity and target density, whose product will be calibrated to 2% accuracy, the detector solid angle, which will be calibrated using the e -p cross section to 1-2%, and the neutron arm detection efficiency, which will be measured to 2-3% accuracy using quasi-elastic electron scattering from deuterium in the target with reduced field in the sweeper magnet (using well-known neutron and proton electromagnetic form factors [41]).

At JLab, the accelerator supplies the electron beams to several halls at the same time. Some of them are using 2 ns bunch structure. As result, the hall with a lower beam rate has a so-called beam “leak”. The fraction of the leak is on the level of 10^{-4} . For example, if Hall A uses 100 μ A, the leak to the Hall C beam line will be 0.01 μ A. The leaking beam also impacts the average beam polarization, which is correctable at least to the level of 10%, so the impact becomes small compared to the projected beam helicity asymmetry (10^{-3}).

Trace deuterium in the hydrogen target will lead to quasi-elastic e -n events, which corresponds to an event rate of 30 Hz for 0.1% contamination and is reduced to 1 Hz by the veto arm. Commercial vendors can supply 100+ times cleaner hydrogen (99.999%), so this type of background will be sufficiently suppressed.

The overall systematics for the relative value of F_A is expected to be below 5%.

The essential part of the experiment concept is the logic of the online trigger and offline analysis. Here, the calorimeters (NCAL in the neutron arm and HCAL in the veto arm) play a key role.

The online triggers will be generated in three steps:

- First, for the proposed kinematics, the kinetic energy of the $p(\vec{e}, n)\nu_e$ neutrons is 526 MeV (for the central angle of the detectors), which allows us to use a relatively high threshold of 100 MeV for the Level-0 online trigger (energy deposited in NCAL and TOF), with modest trigger rate and accurate beam bunch determination while keeping detection efficiency of the neutron arm trigger above 25%.
- Second, a Level-1 trigger will require Level-0 plus wide cuts on correlation of the beam bunch time with neutron hit time in TOF (± 5 ns) and correlation of the hit locations in the TOF and the NCAL (0.25 m^2). It will also exclude a narrow area of time in TOF relative to the beam bunch to remove prompt photon events. This trigger will be generated by the CPU in the front-end electronics, giving a rate below 0.25 MHz.
- Third, a Level-2 trigger will require Level-1 and a tighter geometrical correlation area ($15 \text{ cm} \times 15 \text{ cm}$), reducing the rate to 25 kHz, which is well within the capability of the proposed DAQ, see Appendix B in section XIII. This trigger will also be generated by the CPU in the front-end electronics and allows us to record all information from the TOF, NCAL and HCAL.

The offline analysis event selection will be done in four steps:

- First, the events with a large signal (above 200 MeV) in the veto arm calorimeter HCAL will be removed.
- Second, the cuts on correlations for time and location in TOF and NCAL will be updated with all optimized corrections for position and time reconstruction (± 0.5 ns).
- Third, the TOF and NCAL high accuracy timing data will be used to select the correct beam bunch.
- Fourth, the incident beam energy will be reconstructed by using accurate neutron time-of-flight and scattering angle.

As a part of a test run, studies will be performed on background intensity vs. hit time in a TOF prototype, as well as with the data from an Al target.

From the results of the experiment, the cross section will be calculated as:

$$\frac{d\sigma}{d\Omega} = \frac{(N_+ - N_-)/\eta_n}{P_b \times IL \times \Delta\Omega}, \quad (26)$$

where N_+ , N_- are the number of events for positive/negative beam polarization, each corrected for incident beam charge, η_n is the neutron detection efficiency, P_b is the degree of the beam (helicity) polarization, IL is the integrated luminosity (defined as the product of the beam charge Q (total number of electrons) and target thickness (proton/cm²)), and $\Delta\Omega$ is the neutron detector solid angle.

The relative statistical accuracy for the cross section will be calculated using the total statistics, $(N_+ + N_-)$, and the beam helicity asymmetry for the collected events, $R = (N_+ - N_-)/(N_+ + N_-)$, as:

$$\frac{\Delta\sigma}{\sigma} = \frac{1}{\sqrt{N_+ + N_-} \times R} = \frac{\sqrt{N_+ + N_-}}{N_+ - N_-}, \quad (27)$$

B. Method of the End-point Spectrum

Processes where only one particle in the final state is detected with incident beams of photons or electrons have been used in many experiments including nuclear physics for investigation of energy levels, single pion/kaon production at SLAC [42] and JLab [43], deuteron two-body photo-disintegration at SLAC [44] and JLab [45], proton elastic scattering form factor measurements [46], and others.

To select the process of interest, the parameters of the detected particle are used to calculate the energy of the incident particle. This reconstructed “beam” energy spectrum is used for selection of events near the end-point

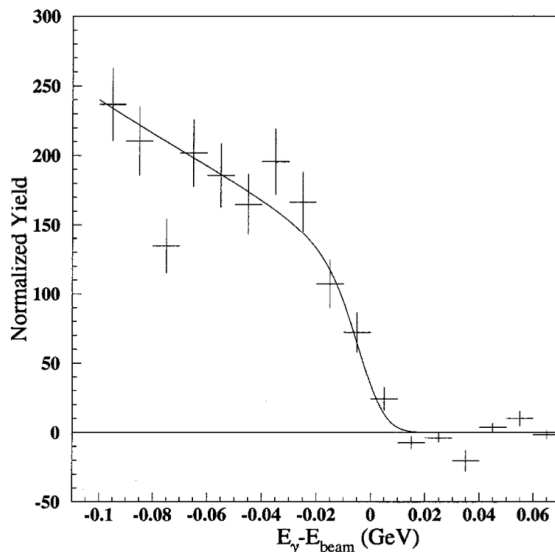


FIG. 13. Event spectrum vs. the reconstructed energy minus the beam energy. Figure is taken from Ref. [43].

(maximum photon energy). An example of such a spectrum is shown in Fig.13, taken from Ref. [43]. Missing mass reconstruction can also be used for selection of exclusive processes when only one particle in the final state is detected.

The equation below shows how the incident energy, E_{beam}^{rec} , is reconstructed for the case of an elastic reaction like $p(\vec{e}, n)\nu_e$.

$$E_{beam}^{rec} = \frac{E_n - (M_p^2 + M_n^2)/2M_p}{1 + (P_n \cos \theta_n - E_n)/M_p}, \quad (28)$$

where E_n and P_n are the neutron energy and 3-momentum determined from the time-of-flight, θ_n is the neutron recoil angle, and M_n and M_p are the neutron and proton masses, resp. The main background process in the proposed experiment is single pion photo-production. For background events, the E_{beam}^{rec} calculated using the formula above is reduced by 43 MeV due to the pion mass (m_π) contribution as shown in the equation below:

$$E_{beam}^{rec} = \frac{E_n - (M_p^2 + M_n^2)/2M_p + m_\pi^2/2M_p}{1 + (P_n \cos \theta_n - E_n)/M_p}. \quad (29)$$

Due to the large distance from the target to the detector (15 m), and a high time-of-flight resolution of 100 ps, the full energy of the produced neutron will be measured with accuracy 3.2 MeV or 0.2% (for a point target). The angular resolution will also be very good, about 1 mrad. From these parameters we calculated that the incident energy reconstruction accuracy will be on the order of 18 MeV, or 1%. The extended target length (10 cm) leads to a significant increase of the time of flight uncertainty (up to 125 ps) and angular resolutions (up to 2 mrad).

The resulting resolution of the reconstructed beam energy is 23 MeV. For determination of the $p(\vec{e}, n)\nu_e$ cross section, we will select events within a 1.4 sigma range at the end-point (from -0.7 sigma to +0.7 sigma) where 50% of the signal events will be located. At the same time, the background processes leaking into this range are strongly suppressed due to the reconstruction accuracy of the incident particle energy.

C. Kinematical parameters of the proposed experiment

The beam energy will be 2.2 GeV with high longitudinal polarization. We assume that beam polarization $P_b = 85\%$. The lab-frame kinematics for elastic scattering are shown in Table I.

Quantity	Variable	Value
Nucleon mass (proton)	m	0.938 GeV
Beam energy	E	2.20 GeV
(Total 4-momentum) ²	s	5.01 GeV ²
-(4-momentum transfer) ²	$-t = Q^2$	1.00 GeV ²
Energy transfer	$\nu = E - E_\nu$	0.53 GeV

Neutron/Proton

Scattering angle	θ_n	48.0°
Energy	E_n	1.47 GeV
3-momentum	p_n	1.13 GeV
Kinetic energy	E_k	0.53 GeV
Beta	β	0.77
Time-of-flight (15 m)	t_n	65.0 ns

Neutrino/Electron

Scattering angle	θ_ν	30.0°
Energy	E_ν	1.67 GeV

TABLE I. The kinematics of the $p(\vec{e}, n)\nu_e$ reaction.

VI. CROSS SECTION AND EVENT RATE OF THE SIGNAL AND BACKGROUND REACTIONS

This section provides the estimated rates of the $p(\vec{e}, n)\nu_e$ reaction and several processes expected to be essential in the proposed measurement. The list of background processes includes elastic and quasi-elastic electron scattering from proton and neutron, pion photo-production, and photo disintegration of p-n pairs. These estimates are accurate to the 20% level and are useful for comparison with the Monte Carlo results. The expected background rates were cross-checked by simulation using Geant4 and FLUKA codes, presented in section VIII.

A. Axial-Vector Form Factor from $p(\vec{e}, n)\nu_e$ process

The rate of the $p(\vec{e}, n)\nu_e$ process for this proposal was obtained in two independent calculations. The first one was made for this proposal by J. Golak. The second one was made with a code written according to P. Kroll's note, see Sec. IV-C. Both calculations found that for a 2.2 GeV electron beam energy, and neutrino production angle of 30° , the cross section, averaged over beam polarization, is:

$$\frac{d\sigma}{d\Omega_{\nu,lab}}|_{e+p\rightarrow\nu+n} = 1.35 \times 10^{-39} \text{ cm}^2/\text{sr} \quad (30)$$

For the proposed neutron detector (the equivalent solid angle for the neutrino is 50 msr) and 10-cm-long LH2 target with 120 μA beam (the luminosity is $3.1 \times 10^{38} \text{ Hz/cm}^2$), the rate, averaged over two polarizations of the beam, is **0.021 Hz**.

The cross section has several contributions and it varies close to linearly with F_A , so the relative accuracy for the Axial-Vector Form Factor is the same as for the cross section.

B. Elastic e -p process

The cross section was calculated from the Rosenbluth formula with the form factors from Ref. [47]. For 2.2 GeV electron beam energy and an electron scattering angle of 30° , the cross section is:

$$\frac{d\sigma}{d\Omega_{lab}}|_{e+p\rightarrow e+p} = 1.4 \times 10^{-32} \text{ cm}^2/\text{sr} \quad (31)$$

For the proposed detector and luminosity ($3.1 \times 10^{38} \text{ Hz/cm}^2$) the rate of e -p events is 223 kHz. The sweeper magnet will remove those primary protons from the acceptance of the neutron arm. However, via charge exchange interactions [48] of the protons in the target side wall (0.20 mm of Al), neutrons will be produced. The Al window of the scattering chamber (0.25 mm) and the air between that window and the sweeper magnet (1 m) also contribute. The combined weight of these three items is 0.25 g/cm². The charge exchange cross section is about 140 mb/GeV² for the forward angles at 500 MeV proton energy [49]. Using the solid angle of the neutron arm of 70 msr, we estimated a cross section of 0.7 mb, and the neutron rate is estimated to be 8.5 Hz. Most of these events (98+%) will be rejected because the scattered electron produces a large signal in the veto arm. In addition, those neutrons obtain an angular spread of up to 4° , giving a wide distribution in the reconstructed beam energy. Estimation shows that less than 15% of these events will be within the 32 MeV region at the end-point in the reconstructed beam energy. This will bring the rate of background neutron events from e -p scattering below **0.02 Hz**.

C. Quasi-elastic electron scattering from Al windows

The cross section for e -p quasi-elastic scattering is $1.5 \times 10^{-32} \text{ cm}^2/\text{sr}$ and for e -n quasi-elastic scattering it is about $0.53 \times 10^{-32} \text{ cm}^2/\text{sr}$. For two Al target windows with a combined thickness of 0.24 mm, the rate of quasi-elastic events from for e -p scattering is about 12.5 kHz and the rate from e -n is about 4.9 kHz. The veto arm efficiency for rejection of neutrons in these events will be on the level of 75+%, even for a wide angular correlation between the scattered electron and recoil nucleon (due to the nucleon Fermi motion), due to the solid angle covered by HCAL (0.4 steradian). A 150-cm thick tungsten collimator will stop all protons and will also reduce the flux of high energy neutrons. We found from FLUKA-based calculations that the reduction factor is about 200.

The energy distribution of the scattered electron has a large width which, for our kinematics, is about 500 MeV, see e.g. Ref. [50]. The recoil neutron also has a similar variation in its kinetic energy. The width of the distribution in the reconstructed beam energy is of order $\pm 600 \text{ MeV}$. The background rate after the cut on the 32 MeV region at the end-point will be on the order of **0.22 Hz**.

D. Pion-neutron photo-production process

This process includes both electro- and photo-production from the LH2 target. The rate calculation for the reaction $p(\gamma, n)\pi^+$ is based on the combined photon flux from Bremsstrahlung and quasi-real photons using the Effective Photon Approximation method (EPA) [51] and data for the pion photo-production cross section from Ref. [52].

The photon energy distribution in the EPA is defined as the number of photons $dn(\omega)$ with energy ω in the range $d\omega$ for each incident electron and is given by:

$$dn(\omega) = N(\omega) [d\omega/\omega], \quad (32)$$

where,

$$N(\omega) = \frac{\alpha}{\pi} \left[\left(1 - \frac{\omega}{E} + \frac{\omega^2}{2E^2} \right) \ln \frac{q_{max}^2}{q_{min}^2} - \left(1 - \frac{\omega}{2E} \right)^2 \ln \frac{\omega^2 + q_{max}^2}{\omega^2 + q_{min}^2} - \frac{m_e^2 \omega^2}{E^2 q_{min}^2} \left(1 - \frac{q_{min}^2}{q_{max}^2} \right) \right], \quad (33)$$

with $q_{min}^2 = m_e^2 \omega^2 / (E(E - \omega))$ and $q_{max}^2 = \min(M_p^2, 4E(E - \omega))$, here $M_p = 770$ MeV.

The quasi-real photon flux in the 75 MeV range from $E_\gamma = 2.20$ GeV down to $E_\gamma = 2.125$ GeV, or $d\omega/\omega = 0.034$, is 3.8×10^{-4} per electron. Real photons due to Bremsstrahlung radiation are produced in 12.5 cm of LH2 (half of the full target length) plus the 0.12 mm Al window of the cell. The total photon intensity (quasi-real plus bremsstrahlung) is 9.1×10^{-4} per electron, and the resulting photon-proton luminosity for the 10-cm-long collimated region of the target is 2.4×10^{35} Hz/cm². The photons outside the selected energy range are not essential for selection of the $p(\vec{e}, n)\nu_e$ events because of good resolution in reconstructed beam energy.

The data for the $p(\gamma, n)\pi^+$ cross section are well-fit by the SAID SP09 (FA07) solution [53] for the range of $E_\gamma = 0.725 - 2.675$ GeV. A pion angle of 65° in the center-of-mass system corresponds to our kinematics with 30° in the lab system. The cross section of pion production for the proposed kinematics is $0.35 \mu\text{b/sr}$ [52]. For a 110 msr solid angle for the pion detection in the center-of-mass system, the projected neutron rate is 11.1 kHz.

Less than 2% of these events will escape rejection by the veto arm due to pion decay with the final muon outside of the HCAL acceptance. The rate of escaped events is about 222 Hz or less. Due to the pion mass, the reconstructed incident energy for these pion-neutron events is shifted by 43 MeV down from the beam energy value, where the neutrino-related events from the elastic CC reaction are concentrated. Based on a Geant4 MC simulation, the accuracy of the incident energy reconstruction is expected to be on the order of 23 MeV. As a result, the leak of the pion-related events into the selected region (-16 to $+16$ MeV) around the end-point will be **0.77 Hz** (from the background rate of this type).

An additional mechanism of background production is due to secondary scattering of the neutron (originated from single pion production) from the protons in the LH2 target. In such a case, a neutron produced with a few degrees outside the neutron arm acceptance could change direction and lead to an event with a large reconstructed beam energy. For example, for $E_\gamma = 2200$ MeV when the pion is produced at 35 degrees, the neutron is produced at 44 degrees with kinetic energy 655 MeV (momentum 1.3 GeV/c). Scattering from the LH2 proton by 1 degree will bring the neutron into the neutron arm acceptance with almost the same 655 MeV energy because the recoil proton energy is just 0.4 MeV. The reconstructed beam energy will be higher than the threshold for pions (2200-43 MeV) by 150 MeV. So, the events from the corresponding solid angle will be distributed over a 150 MeV range, including the 32 MeV range where neutrino events are located. The cross section of $n - p$ elastic scattering for a 655 MeV proton is 8 mb/sr [53] for a small scattering angle, which leads to the probability of re-scattering in the LH2 of 7×10^{-5} or, a rate in the neutron arm of 9 Hz. Veto rejection will reduce the relevant number of events to 0.18 Hz, out of which less than 15% will be in the E_{rec} window of neutrino events. Thus, the estimated rate of this type of background is **0.04 Hz**.

E. Pion-neutron photo-production from Al target windows

There are two processes with a pion and a neutron in the final state, $\pi^+ - n$ or $\pi^0 - n$, which lead to production of high energy neutrons from the Al target windows. The photon intensity relevant to this type of background is much larger than it is in the case of hydrogen because of the Fermi motion of the proton in Al. As a result, photons with energy even as low as 1900 MeV can produce high energy neutrons for which the reconstructed incident energy is in the area near the end-point where the events from $p(\vec{e}, n)\nu_e$ are located.

The photon flux (averaged between two windows), in the range of 1900-2200 MeV, is 3.5×10^{12} γ /s (sum of quasi-real and real photons). The number of protons in both Al windows is 20 times lower than in the hydrogen target and there are a similar number of neutrons. The resulting photon-nucleon luminosity is 2.0×10^{35} **Hz/cm²**. This corresponds to a neutron production rate of 6.7 kHz. The protons are removed completely by the collimator and the sweeper magnet. There are two big reduction factors for these type of neutrons: The first one is due to absorption in the tungsten collimator (a factor of 200) and the second one is from the cut on the reconstructed incident beam energy (a factor of 35). An additional reduction by a factor of 10+ is expected by using the veto arm which will detect π^+ and γ 's from π^0 decay. The resulting suppression factor is expected to be $\sim 50,000$. The total rate of this type of event is expected to be on the order of **0.16 Hz**.

F. Neutron-proton photo-production from Al windows

The dominant mechanism of the $\text{Al}(\gamma, p n)X$ process is disintegration of a proton-neutron pair. At lower photon energy, the process is described by the well-known Levinger factor [16]. In the regime of a few GeV, the momentum distribution is different and was measured [54]. In the 2-4 GeV energy range, there were several experiments on $\text{D}(\gamma, p)$ at SLAC and JLab [44, 45]. As a by-product, the cross section for $\text{Al}(\gamma, p)$ was also obtained. For a photon energy of 1950 MeV, the cross section was estimated to be of order 100 nb/sr [55]. The corresponding counting rate is 10 Hz. After reduction by the tungsten collimator, the rate is reduced below 0.05 Hz. With the cut on the reconstructed beam energy, the rate falls below **0.01 Hz**.

G. Summary of the rate estimates

As was shown above, the signal rate is 0.021 Hz and the combined background rate is 1.22 Hz. In a 50-day run, the total number of signal events will be 9.55k (taking into account the 25% efficiency, combined TOF+NCAL in energy threshold and bunch determination, the loss of 50% of the good signal events due to a -0.7 to +0.7 sigma cut on the reconstructed beam energy, and 85% polarization of the beam). Background statistics in the 32 MeV range of E_{rec} is expected to be about 1.32M (also corrected for 25% detection efficiency). From these values, the $(N_{+/-})$: $R = (N_+ - N_-)/(N_+ + N_-)$, $R = 7.2 \times 10^{-3}$, and the projected accuracy of the $p(\vec{e}, n)\nu_e$ cross section was estimated to be close to **12%**.

However, this result does not include the background due to two-pion photo production process with an $n + \pi^+ + \pi^0$ final state. There is no experimental data on this reaction for photon energy above 1 GeV. We used a Geant4 prediction to evaluate the rate of related events and calculate the potential impact on the F_A measurement accuracy, see **the final result in sec. VIII**.

VII. EXPERIMENTAL SETUP

A. Overview

The experiment will be installed in Hall C using the geometry as shown in Figure 14. The 25-cm-long liquid hydrogen target, at a pivot located 7.2 m downstream of the main pivot, will be used along with tungsten collimators limiting the visible target length to 10 cm, which is needed to provide the necessary timing resolution. The collimation also suppresses events produced in the Al windows of the liquid hydrogen cell.

We will be detecting neutrons from the elastic weak CC interaction, referred to here as “primary neutrons”, in the presence of two dominant background processes: 1) recoil protons from elastic $p(\bar{\nu}_e, p)e'$ scattering and 2) neutrons from pion photo-production. The rates from these backgrounds are $10^7 - 10^8$ times larger than the rate from primary neutrons. The experiment will use two spectrometers, referred to as the neutron arm and veto arm. The $120 \mu\text{A}$ beam will have energy of 2.2 GeV and high longitudinal polarization. It will be delivered in bunches, each 2 ps wide, every 8 ns.

The neutron arm includes a sweeper magnet with a vertical magnetic field located at a distance of 1.5 m from the target at an angle of 48° on the beam-right side. Elastic recoil protons and all other charged particles will be swept off the acceptance of the neutron detector.

The neutron detector package includes a time-of-flight detector, TOF, at a distance of 15 m from the target. The TOF is made of a stack of 6 cm x 6 cm x 200 cm scintillator bars used for determination of the time-of-flight and hit location. This is followed by a well-segmented neutron calorimeter, NCAL, at a distance of 17.5 m from the target. Neutron hits in TOF and NCAL are separated by 2-2.5 m, which allows us to find the speed of the primary neutron to 3% accuracy and identify the beam bunch. The main purpose of NCAL is to provide a Level-0 trigger by detecting events above 100 MeV that are correlated with a beam bunch.

The veto arm includes eight layers of GEM chambers and the Hadron Calorimeter (HCAL) to veto background events by detecting recoil electrons (e -n events) and pions (π -n events). The calorimeter front face will be at a distance of 4 m from the target. The total solid angle of the veto arm is 0.4 steradian, which is essential for effective vetoing of the background. The detectors of SBS already exist and were used in the SBS form factor program in Hall A. This arm will also be used for calibration of TOF and NCAL by detecting scattered electrons in coincidence with protons in NCAL (sweeper magnet off) from the elastic e -p reaction. The veto arm will be located at an angle of 30° on the beam-left side.

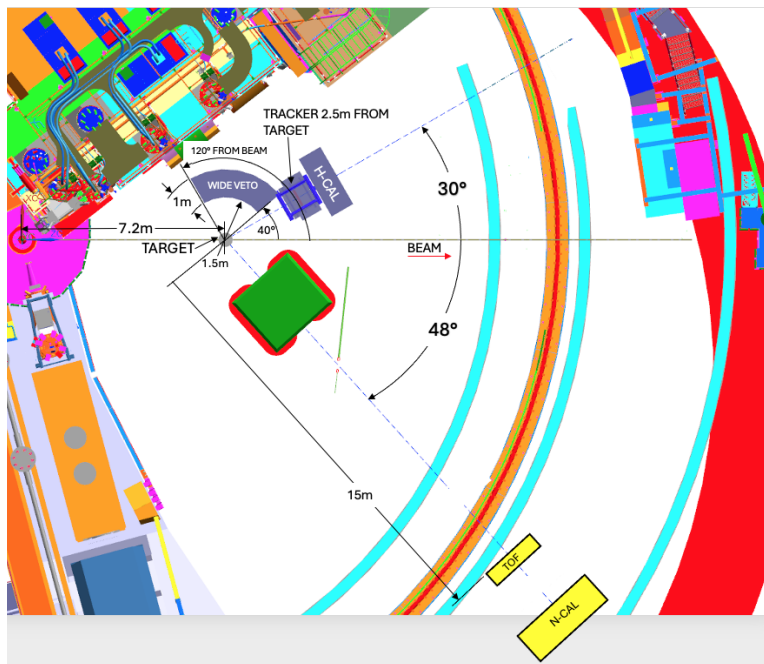


FIG. 14. Hall C design for the AVFF experiment.

B. Neutron Arm

1. Sweeper Magnet

A room-temperature dipole magnet will be installed near the target at an angle of 48° , with a distance of 3 m from the target to the magnet center. The field integral along the neutron trajectory will be of order 1 T-m. The magnet design is shown in Figure 15. It consists of water-cooled copper coils wound around iron yoke bars. The required current in the coil is 2000 A. The horizontal opening is $\pm 6^\circ$ for neutrons. The vertical field along the neutron trajectory through the center of the bore (z direction) is shown in Figure 15-Right. The vertical opening in the magnet is a little bit larger on the negative z side to accommodate the required vertical angular range.

The stray field at the beam line reaches 150 G. To compensate for beam steering, we require soft iron shielding and two corrector magnets as shown in Figure 15-Left. The details of the corrector magnets are available.

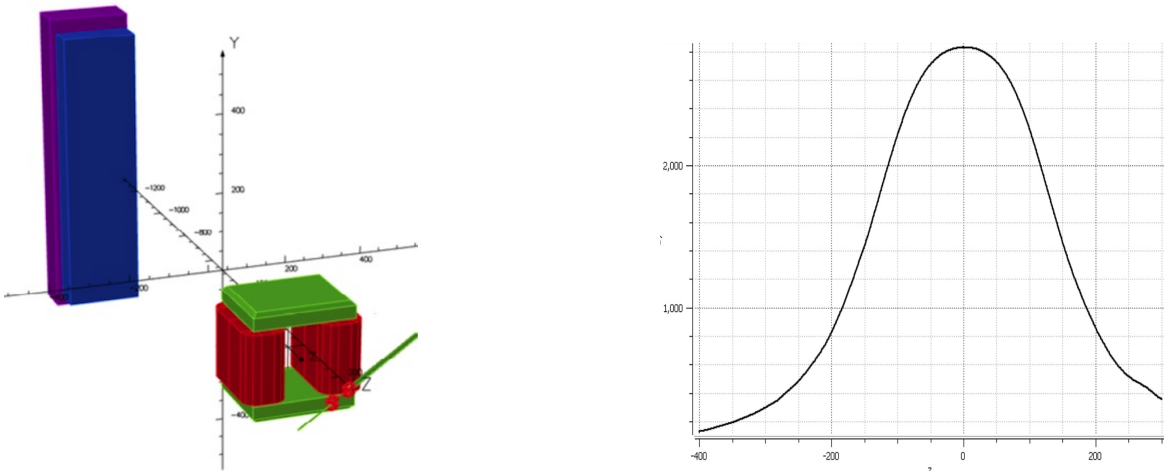


FIG. 15. Left: Sweeper magnet configuration. Left: The origin (0,0,0) is located at the center of the bore. Coordinate units are centimeters. The sweeper is shown as a large green iron yoke with red coils. Beam electrons travel from the left, along the green line in front of the sweeper. The correctors are the smaller red coils located on the beamline in front of the sweeper. The blue and purple rectangles are the TOF and NCAL detectors, resp. Right: The vertical component of the sweeper field B_y . The horizontal axis is the distance from the magnet center in centimeters; the vertical axis is the magnetic field in Gauss.

2. The Time-of-Flight Detector

A time-of-flight detector (TOF) will be used to measure neutron speed to allow separation of events from the reaction $p(\vec{e}, n)\nu_e$ from those due to pion photo-production which are, in reconstructed beam energy spectra, at least 43 MeV below 2200 MeV, where $p(\vec{e}, n)\nu_e$ events are located. The signal events have about 0.2% neutron energy resolution with expected 100 ps TOF resolution, corresponding to 23 MeV resolution for reconstructed beam energy. Measurement of the time-of-flight requires determination of the correct beam bunch, which we will do by detecting the same neutron in TOF and NCAL. The front of the TOF will be 15 meters from the target, followed by NCAL at 17.5 meters from the target. Thus, the speed of the neutron will be measured with a few percent accuracy, which allows us to select the proper beam bunch.

The TOF detector will include 11 planes, each of them having 140 bars arranged vertically (a total of 1540 bars). The bar dimensions are 6 cm x 6 cm x 200 cm (W x H x L) with a 2" diameter PMT on each end. To achieve the required timing resolution we will use BC-408 scintillator material identical to that used for the CLAS12 forward TOF detector system [56], see Table II. Figure 17 shows the timing resolution achieved with these bars for ~ 10 MeV energy deposition in the scintillator (minimum ionizing particles). For efficient detection of the neutron, the threshold on energy deposition in TOF needs to be on the order of 3 MeV, for which the time resolution will be about 1.8 times larger. An additional contribution of 60 ps comes from variation of the time of the neutron interaction within a single TOF bar. The combined resolution will be 110 ps for a 2 m long bar. A detailed description of the DAQ for the TOF is given in Sec. XIII-B.

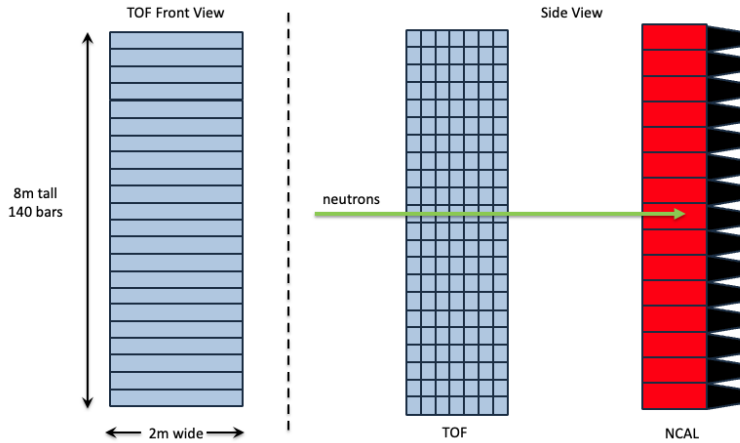


FIG. 16. Schematic of the TOF detector (blue) consists of 11 planes, each of them having 140 bars arranged vertically. Each bar has dimensions 6 cm x 6 cm x 200 cm (H x W x L) with a PMT attached to each end. Approximately 2-2.5 meters following the TOF, shown in red, are the NCAL modules with PMTs in black. Note: For clarity, the actual number of TOF bars and NCAL modules is not shown.

Property	BC-408
Light Output, % Anthracene	64
Rise Time (ns)	0.9
Decay Time (ns)	2.1
Pulse Width, FWHM (ns)	2.5
Wavelength of maximum emission (nm)	425
Light attenuation length (cm)	210
Bulk attenuation length (cm)	380
Polymer base	Polyvinyltoluene
Refractive index	1.58
Density (g/cm ³)	1.023

TABLE II. Specifications for BC-408 scintillator material. Data taken from [56]

3. The Neutron Arm Calorimeter

The neutron arm calorimeter, NCAL, will have an active area of about a 30 m², giving a solid angle of 70 msr at a distance of 17.5 m from the target, and will detect neutrons, which are scattered in the TOF detector. For the design of our calorimeter modules, we selected the modules used in the BNL-E864 calorimeter [57] which have good energy resolution ($3\% + 34\%/\sqrt{E[GeV]}$) and superior time resolution (0.4-0.5 ns). The availability of some E864 modules, enough for a 4.5 m² calorimeter, has been confirmed.

C. Veto Arm

The veto arm will be located at 30° to detect scattered electrons from $e-p$ elastic scattering and π^+ associated with a neutron in single pion photo-production. Using the sweeper magnet described above, we expect to have no elastic protons in the neutron arm. It will, however, have a high rate of neutrons from pion photo-production. Detecting the recoiling pion will allow us to veto most of these events.

In veto mode, the spectrometer will use the Hadron Calorimeter, HCAL, from the SBS spectrometer. The front face of the HCAL is located 4 m from the target center.

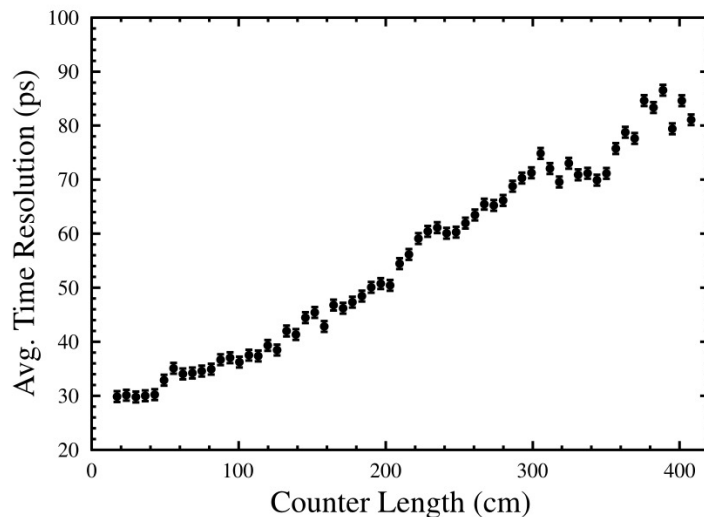


FIG. 17. The time resolution vs. counter length achieved on the benchtop using cosmic rays by the CLAS12 TOF group. Our experiment will use 200 cm bars which have a time resolution of 50 ps for cosmics with a 10 MeV threshold. Our calculation shows for a threshold of 3 MeV, the resolution will be 1.8 times larger, ~ 100 ps. Figure taken from [56].

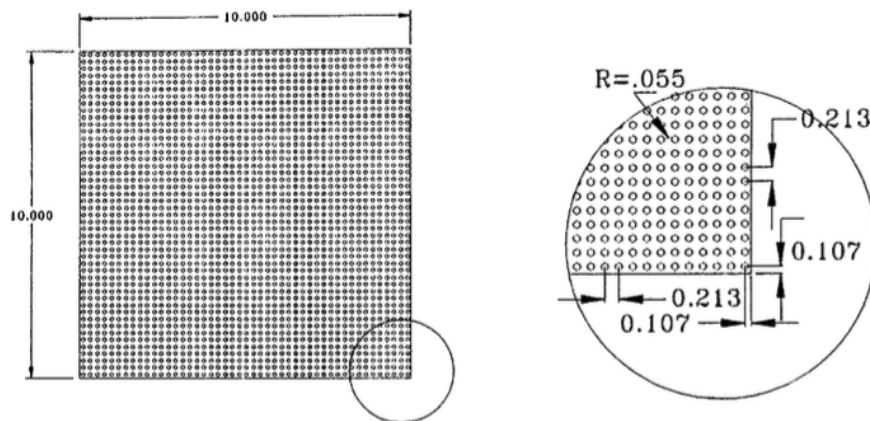


FIG. 18. E864 calorimeter module section.

1. GEM tracking detectors

This arm will also be used for energy calibration and to study the spatial resolution of NCAL using the elastic e - p reaction. The beam current will be reduced and the sweeper magnet turned off. Eight layers of GEM detectors will be used to determine the trajectory of the scattered electrons. These are GEMs that have been used in the Hall A SBS form factor program, the details of which are taken from the doctoral thesis of Sean Jeffas [58]. Construction, operation and DAQ details may be found in his thesis as well. The geometry and placement of the GEM chambers are matched to the acceptance of the SBS/HCAL system. For GEMs measuring in the XY geometry, the position resolution for a single plane is $50 \mu\text{m}$. For the UV geometry it is $100 \mu\text{m}$. At high luminosity, the track efficiency, defined as the probability for a good track to be found for a given trigger using a minimum of three GEM planes, was above 95%. The challenge with the GEMs was the high luminosity of the experiment due to the small cross section of the process. For our calibration, we will run with luminosity approximately an order of magnitude smaller due to the relatively large e - p cross section.

2. Veto Arm Calorimeter

The SBS hadron calorimeter, HCal, was used in the first group of Hall A SBS experiments to detect recoil protons and neutrons in quasi-elastic scattering from deuterium and ^3He . See Figure 19. In the experiment proposed here, it will be used for detecting electrons and pions coincident with neutrons and protons in the neutron arm. It consists of 288 modules as described in Sec. VII B 3.

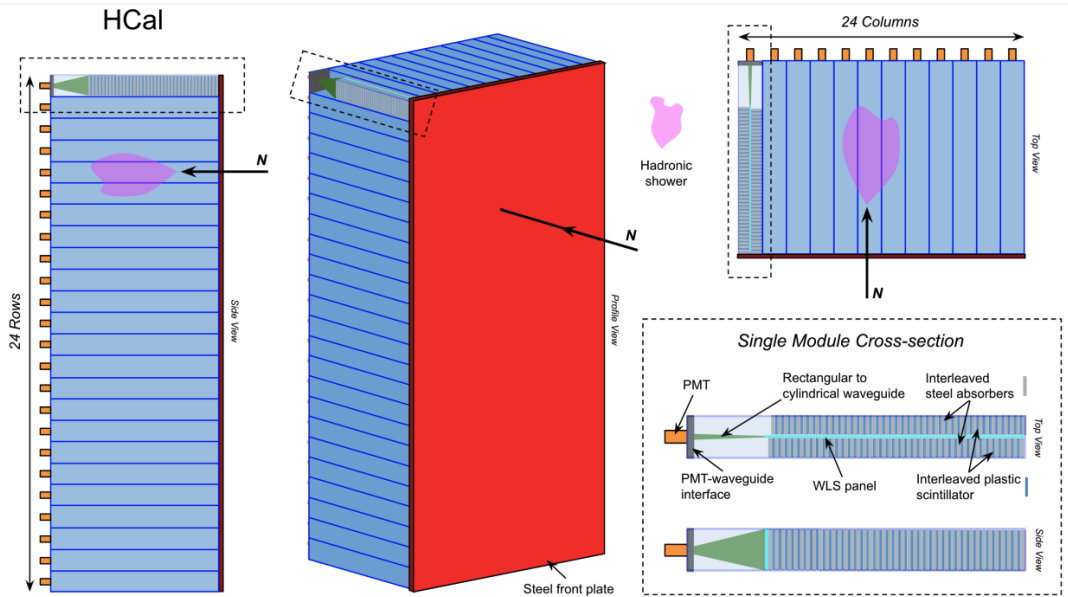


FIG. 19. The HCal detector as used in the Hall A SBS program consists of 12 columns and 24 rows of iron/scintillator modules. The size of the detector is 180 cm x 360 cm, W x H. Each module contained 40 layers of alternating iron and scintillator. Light was transported via wavelength-shifting plastic sheets to light guides to PMTs. Figure taken from [59].

3. “Wide Veto” Calorimeter

An additional calorimeter will be used on the veto arm side of the beam for detection of the photons, pions, and protons associated with two-pion production. That calorimeter will be installed at a distance of 1.5 meters from the target and cover a wide range of polar angles from 40 to 120 degrees with a total solid angle of 2 steradian.

D. Target

We plan to use a cryogenic target with a vertical flow in an Al cell with a 2 cm horizontal width. The full length of the cell is 25 cm. The side walls will have a thickness of 0.20 mm. The beam windows will each have a thickness of 0.12 mm.

E. Beam

The neutrons of interest for this experiment will arrive at the TOF 65.2 ns after production at the target. The time-of-flight for photons is 50 ns. We require a beam bunch (RF) spacing of 8 ns based on the projected neutron speed resolution of the proposed TOF-NCAL system. We plan to use a 120 μA beam with a pulse rate of 125 MHz, which is deliverable by the accelerator [60, 61]. The length of an electron bunch corresponds to a time spread of 2 ps. Note that in 2004, the G0 experiment [26] successfully ran with a 32 ns pulse rate with a current of 40 μA .

VIII. MONTE CARLO SIMULATIONS OF THE EXPERIMENT

A. Overview

This section presents the calculations of the rates in the detector components based on simulations using FLUKA and Geant4.

The neutron arm will be installed at 48° with a solid angle of 70 msr at a distance of 15 m (TOF) from the target. The detectors in the neutron arm are an array of scintillator counters (TOF) and a segmented hadron calorimeter (NCAL) located 2.5 meters beyond the TOF. The veto arm is at 30° on the other side of the beam line and its total solid angle is 400 msr (only 50 msr is required for e -p events). The veto arm consists of the GEM chambers and the hadron calorimeter (HCAL). Additionally, a “wide veto” calorimeter will be at a distance of 1.5-2 m from the target and cover a polar angle range of 40-120 degrees with a 2 steradian solid angle.

The energy threshold for a signal in a single TOF bar will be 3 MeV to allow for 100-ps time resolution and 5% neutron detection efficiency. A much higher 100 MeV threshold will be used for the combined energy deposition in the NCAL cluster plus energy deposition in TOF, correlated in time and position with the NCAL cluster. An additional condition for event selection comes from measurement of the neutron speed between TOF and NCAL, for which the cuts are the hit with energy deposition above 3 MeV in TOF and the speed between a TOF layer and NCAL, $v/c > 0.6$. For the conditions above, the detection efficiency in the neutron arm was found to be of order of 25%.

We will use a 2.2 GeV beam at $120 \mu\text{A}$ on a 25 cm liquid hydrogen target. The target will be collimated using tungsten to limit the visible region to the middle 10 cm. Only a very small fraction of the neutrons from the aluminum cell end-windows will penetrate the collimator and arrive at the detectors.

B. FLUKA based results

Rate results presented in Figs. 20-Left and 21 were produced by P. Degtiarenko (JLab), using FLUKA 2024.1.3 for a 20 cm-long LH2 target. The rates in the angular range of the neutron arm are shown in Figs. 20-Right, for the LH2, Al windows, and combined.

1. Neutron Rates

From these plots, interpolating to a 10-cm-long liquid hydrogen target, we find the following hit rates for a beam current of $120 \mu\text{A}$:

1) In a single TOF bar (0.53 msr solid angle) with E_{dep} above 3 MeV, the rate of detected neutrons will be on the order of 20 kHz (5% detection efficiency).

2) In an area 0.25 m^2 (1.1 msr solid angle), using the full thickness of the TOF (11 layers), with E_{dep} in a single bar above 3 MeV, the rate of detected neutrons will be 330 kHz (40% detection efficiency).

3) In an NCAL cluster (3x3 blocks, 1 msr solid angle) with E_{dep} above 100 MeV (use the Right plot in Fig. 20), the rate of detected neutrons will be 100 kHz.

With a 10 ns time coincidence window, the rate in a 0.25 m^2 TOF and NCAL cluster area is 330 Hz. For the full area of NCAL we need to take into account 64 independent cluster areas, so the rate is 21 kHz. However, the overlap between NCAL areas will double the number of combinations, giving a final estimated of the accidental coincidence trigger rate of **42 kHz**. Note that the real coincidence rate from pion/electrons related neutrons will be **12 kHz**, see sec. VI.

2. Photon Rate

A similar analysis was done for the rate induced by the photons using FLUKA results, shown in Fig. 21. Note that these photons will be completely removed at the trigger level because they will be outside our neutron timing cut. Secondary neutrons induced by these photons have an extremely low rate.

From these photon rates, interpolating to a 10-cm-long liquid hydrogen target with two $120 \mu\text{m}$ Al windows, we find the following hit rates for a beam current of $120 \mu\text{A}$:

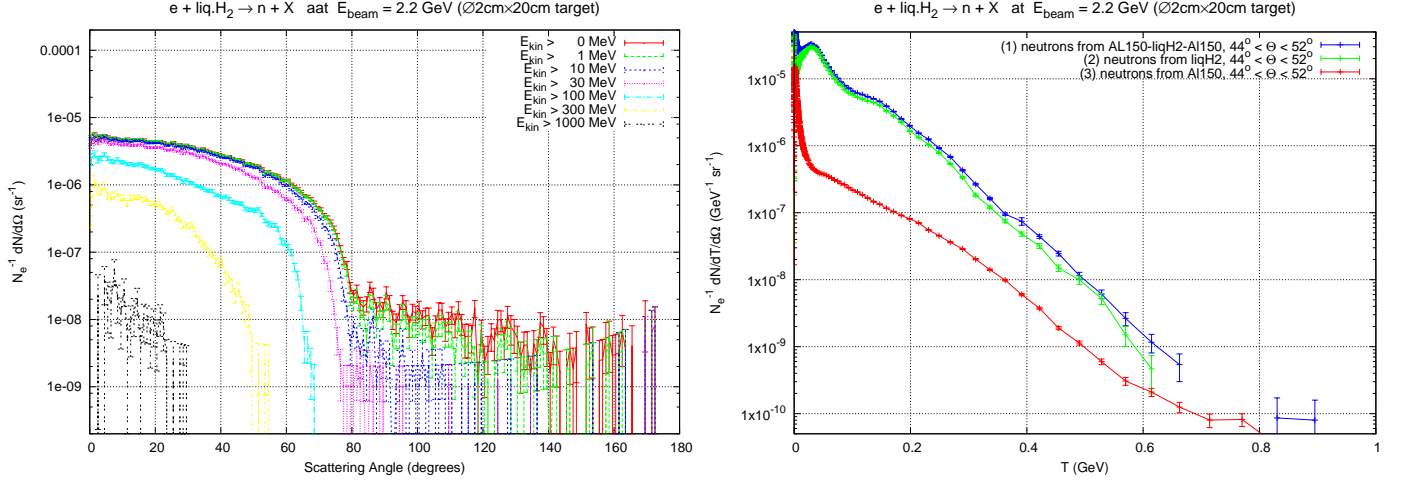


FIG. 20. Left: FLUKA simulation of the neutron rate (Hz/sr) per incident electron for the reaction $e^- + \text{LH}_2 \rightarrow n + X$ for a range of kinetic energies above a given threshold, as a function of laboratory scattering angle assuming a 20 cm target. Right: FLUKA simulation of the neutron rate (Hz/GeV/sr) per incident electron assuming 150 μm of Al, 20 cm liquid hydrogen and combined total rates.

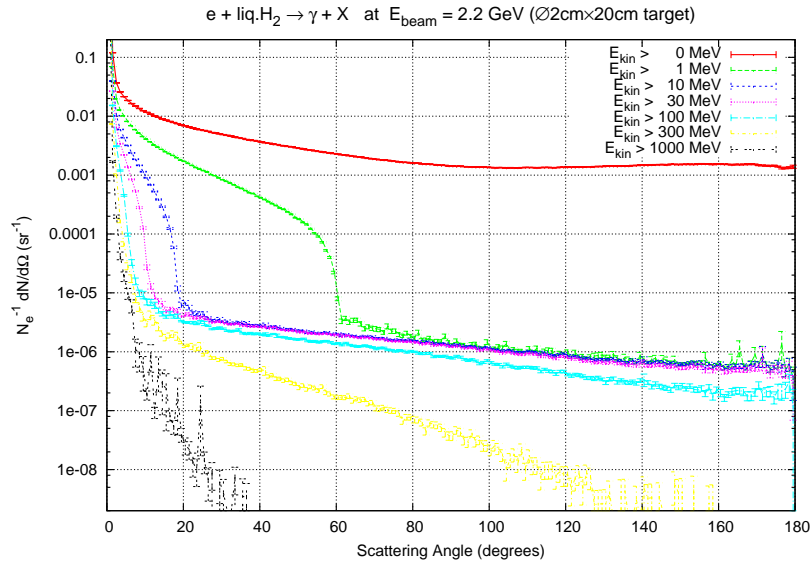


FIG. 21. FLUKA simulation of the photon rate (Hz/sr) per incident electron for the reaction $e^- + \text{LH}_2 \rightarrow \gamma + X$ for a range of energies above a given threshold, as a function of laboratory scattering angle for a 20 cm target.

- 1) In a single TOF bar (0.53 msr solid angle) with E_{dep} above 3 MeV, the rate of detected photons will be on the order of 190 kHz (including 10% projected efficiency due to e^+e^- pair). Due to a 20 ns time window for L-R coincidence in single TOF bar, the accidental rate will be 0.3 kHz, which is much less than the real coincidence rate.
- 2) In an area 0.25 m 2 (1.1 msr solid angle), the full thickness TOF (11 layers) with E_{dep} above 3 MeV in a single bar the rate of detected photons will be 3 MHz (including a 75% projected efficiency).

3) In a cluster (3x3 blocks) of NCAL (1 msr solid angle) with E_{dep} above 100 MeV, the rate of detected photons will be 350 kHz.

With a 10 ns time coincidence window around the photon peak relative to the beam bunch time, the rate in a 0.25 m^2 TOF and NCAL cluster area is 11 kHz. For the full area of NCAL, we need to take into account 64 independent cluster areas, so the rate is 700 kHz. However, the overlaps between NCAL areas will double the number of combinations and rate to 1.4 MHz. Already at the Level-1 trigger, we will exclude most of the prompt photon events because they are well synchronized with the beam bunch

C. Geant4 based results and comparison with FLUKA

Results produced by W. Xiong for the same beam and target parameters using Geant4 are presented here in Figs. 22 and 23.

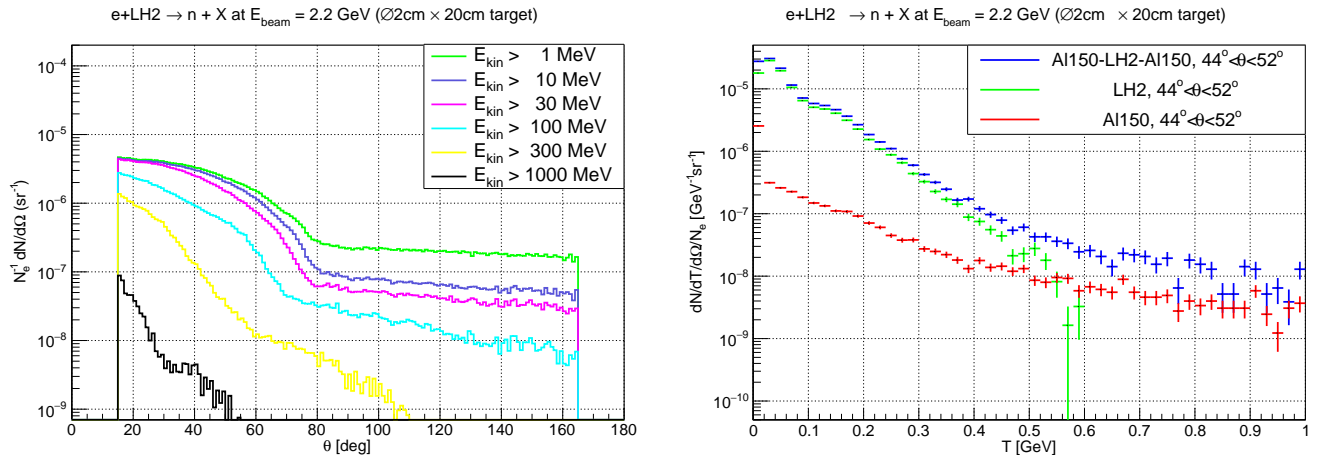


FIG. 22. Left: Geant4 simulation of the neutron rate (Hz/sr) per incident electron for the reaction $e^- + \text{LH}_2 \rightarrow n + X$ for a range of kinetic energies above a given threshold, as a function of laboratory scattering angle assuming a 20 cm target. Right: Geant4 simulation of the neutron rate (Hz/GeV/sr) per incident electron assuming 150 μm of Al, 20 cm liquid hydrogen and combined total rates.

When we compare FLUKA results shown in Fig. 20-Right with those from Geant4 in Fig. 22-Right, we find reasonable agreement for low neutron energies (up to kinetic energy $T \sim 0.3 \text{ GeV}$) which confirms the rates presented above. However, at $T \sim 500 \text{ MeV}$, Geant4 gives a neutron rate from LH2 **two times larger** and from Al, ten times larger with much smaller T dependence. Our analytical calculations of the rate on the LH2 target for 500 MeV neutron kinetic energy agree well with the FLUKA result.

The probability of neutron penetration through the 50 cm tungsten collimator was investigated using both FLUKA and Geant4. The results are in reasonable agreement, see Fig. 24.

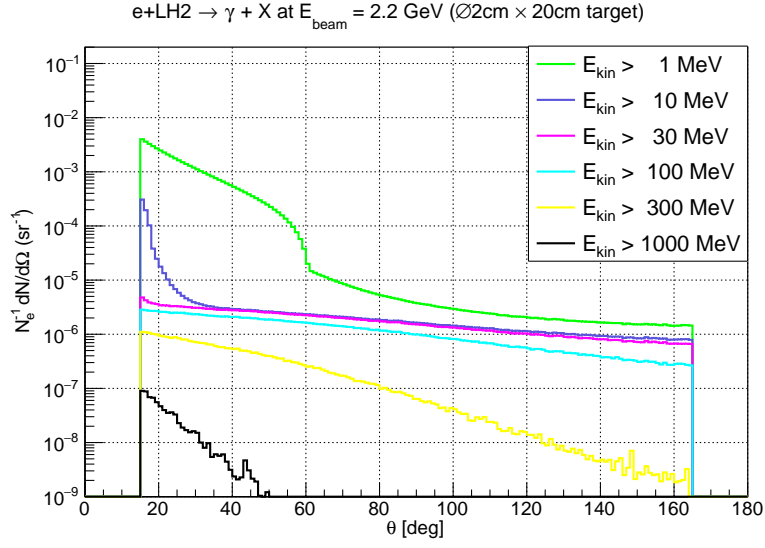


FIG. 23. Geant4 simulation of the photon rate (Hz/sr) per incident electron for the reaction $e^- + LH2 \rightarrow \gamma + X$ for a range of energies above given threshold, as a function of laboratory scattering angle for a 20 cm target.

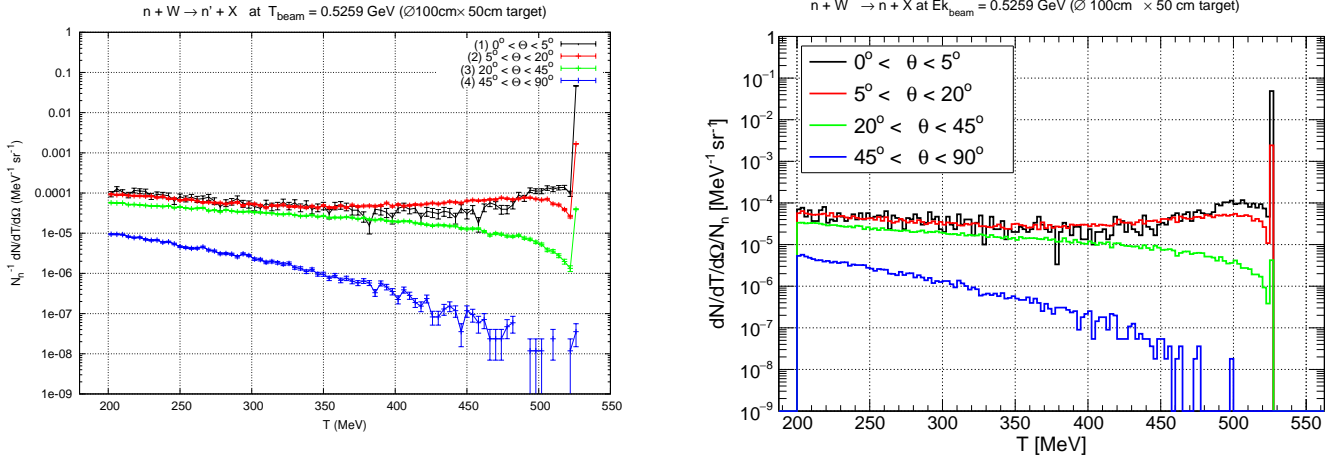


FIG. 24. Left: FLUKA simulation of the neutron rate (Hz/sr) per incident neutron in 50 cm thickness tungsten block. Right: Geant4 simulation of the neutron rate (Hz/GeV/sr) per incident neutron in 50 cm thickness tungsten block.

D. Monte Carlo simulation of the experiment in Geant4 framework

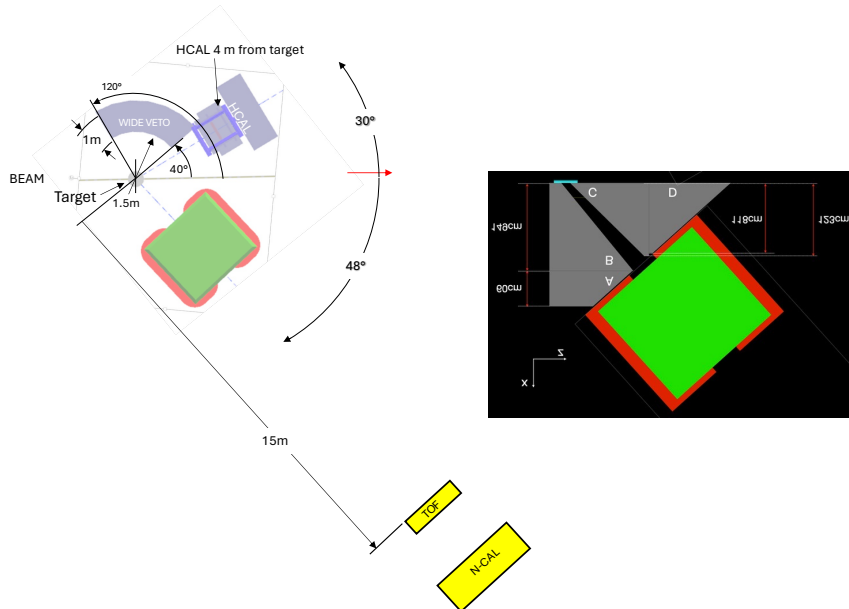


FIG. 25. Top view of layout used for the Geant4 model. Insert: View of the target area with the tungsten collimator in Geant4.

For this experiment the Geant4 simulation package was developed based on G4SBS. The layout of the full experimental setup used in the Geant4 model is shown in Fig. 25. In addition to the SBS-based veto arm, it contains a detailed description of the neutron arm, including the sweeper magnet and neutron TOF detector, as well as the neutron calorimeter, with geometric and material information exactly as described in chapter VII. The simulation includes also a tungsten collimator and shielding between the target chamber and the sweeper magnet to reduce neutron background generated from the aluminum cell windows and, a shielding wall to block neutrons generated along the beampipe.

The energy of the neutrons will be measured using both calorimetry and time-of-flight. For the calorimetry method, we combine the energy deposition in both the TOF scintillators and NCAL, as:

$$T_{recon}^{cal} = a \cdot E_{tof} + b \cdot E_{NCAL}, \quad (34)$$

where a and b are calibration constants that can be obtained from fits. The neutron energy in NCAL+TOF will be used as the Level-0 trigger.

Using the Geant4 model, MC simulations were made. The result for NCAL energy resolution can be seen in Fig. 26-Right. The result for the efficiency at the conditions of the signals in NCAL+TOF above 100 MeV, and with a correlated TOF hit, is 25%. The kinetic energy of neutrons will be determined precisely from the TOF data. Assuming a 100 ps time resolution for the TOF counters, the resolution for neutron energy is 3 MeV. The reconstructed incident beam energy, E_{rec} , has a resolution of 23 MeV. The event distribution for the single pion production processes is shown in Fig. 26-Left. The expected shift of the single pion events down from the elastic peak area is easily visible.

The event distribution of detected neutron energy vs. angle, shown in Fig. 27, has a tail well above the dominant band related to single pion production. The events above the band are mostly due to the two-pion process, $\gamma p \rightarrow n \pi^+ \pi^0$. The 2D distribution of the pion energy vs. angle in the veto calorimeters for this type of events is shown in Fig. 28. Many of these events will be vetoed by a “wide veto” with a solid angle of 2 steradians and an optimized energy threshold depending on the angle.

The method of beam bunch determination is based on measurement of the neutron time-of-flight between the TOF and NCAL. The results of the MC simulation of the neutron speed are shown in Fig. 29 and Fig. 30. Selection of the events with a signal in TOF above 3 MeV, neutron v/c above 0.60, and signal in NCAL above 100 MeV leads to a combined efficiency of 25% for events of interest and also provides the neutron speed with a relative accuracy of 3.6%, which is sufficient for determination of the bunches separated by 8 ns.

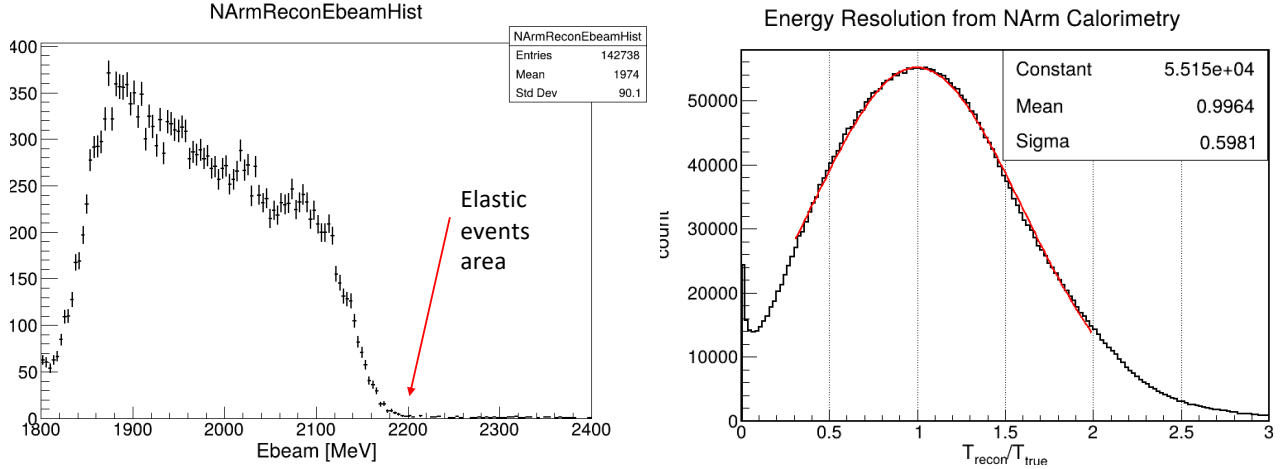


FIG. 26. Left: Geant4 simulation of the reconstructed incident beam energy. Note that the primary photons with energy below 1.9 GeV were not included in MC. Right: Geant4 simulation of the NCAL energy resolution (with HCAL module design).

The full MC simulation of experiment was done using a photon beam, normalized to the intensity equivalent of a $120 \mu\text{A}$ electron beam, including contributions from both the real and quasi-real photons. The generated events have information from TOF, NCAL and the “wide veto”, including the time, location, energy deposition for every hit. Thresholds on the TOF signal amplitude (3 MeV) and NCAL+TOF energy deposition (100 MeV) were

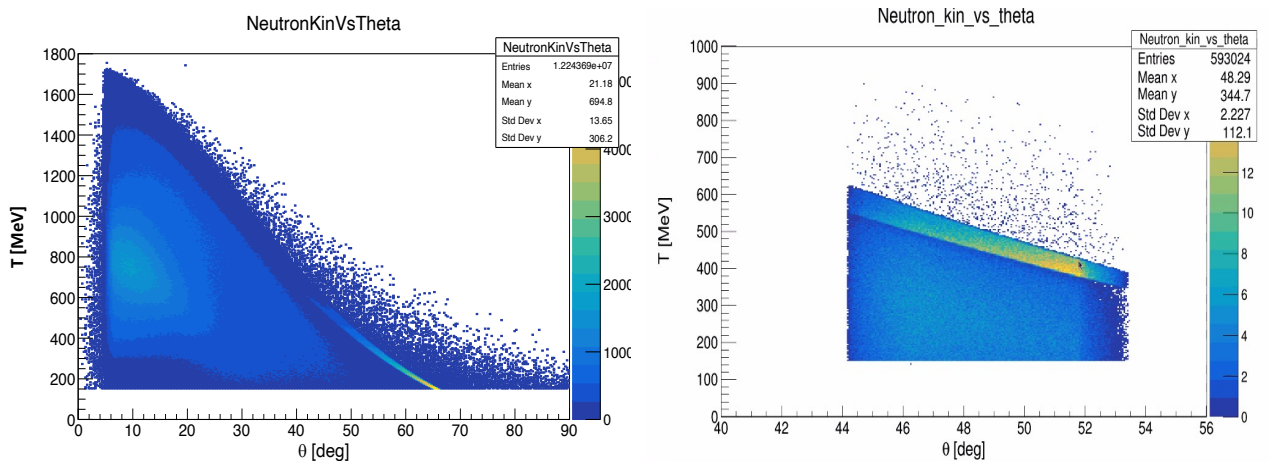


FIG. 27. Left: Geant4 simulation of the neutron energy vs. angle. Right: The same for the detected neutrons.

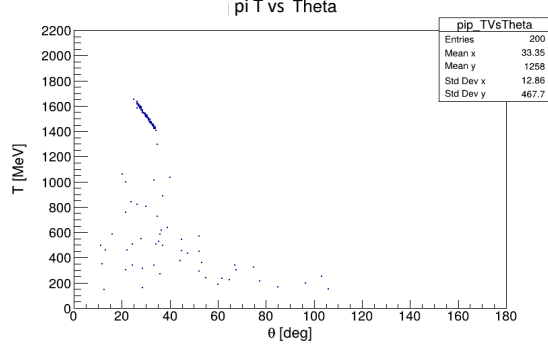


FIG. 28. Distribution of pion hits (pion energy vs. pion angle) in the veto arm side.

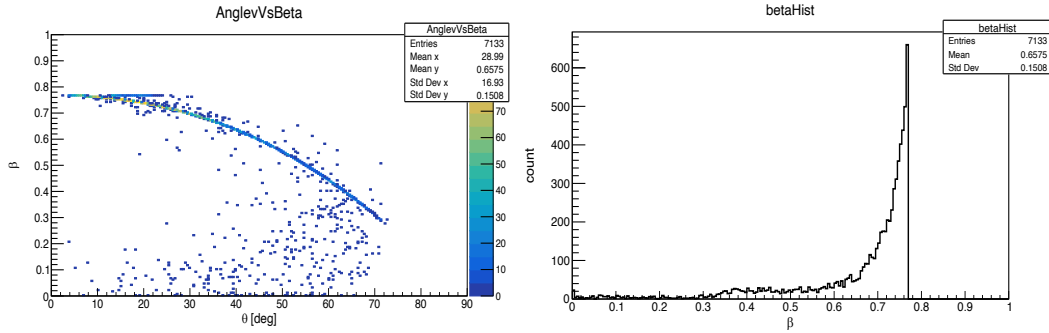


FIG. 29. Left: Geant4 simulation of the speed, β , versus angle of neutrons scattering in TOF. Right: Speed (β) distribution of neutrons after scattering in TOF.

applied. Next, the data were analyzed for the neutron angle and energy and were used to calculate the incident beam energy. Such an analysis allows us to calculate the event rate within the range of $p(\vec{e}, n)\nu_e$ events: 2200 ± 16 MeV.

The result for the background rate (beyond the single pion process) was found to be **11.8 Hz** without the use of the “wide veto” calorimeter information. The efficiency of the “wide veto” counter is defined by its solid angle and energy threshold. For a 100-400 MeV threshold (depending on the angle) and the proposed solid angle, the efficiency was found to be 50% but the counting rate is on the order of 100 MHz. Because of the high rate, we decided to use 11.8 Hz: a conservative estimate of the background which does not rely on “wide veto” information.

We’d also like to note that, as shown above, the rate of high energy neutrons (500+ MeV) from the LH2 target obtained in Geant4 is twice as high as those obtained by FLUKA. Due to such a difference, the double-pion event rate obtained in the Geant4 MC could be overestimated by a factor of two. If this the case, the accuracy on F_A is almost $\sqrt{2}$ better.

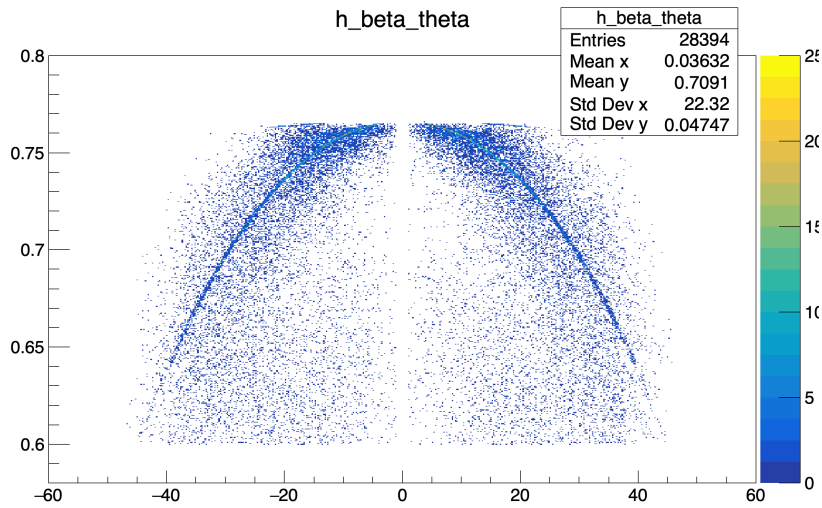


FIG. 30. Geant4 simulation of the neutron speed, β , versus angle (deg) after interaction in one layer of the TOF. Plot from M. Ungaro.

E. Summary of MC result on projected accuracy

With the parameters presented in this section, and 11.8 Hz of background rate, the helicity asymmetry, $R = (N_+ - N_-)/(N_+ + N_-)$, becomes much less than was found in sec. VI. Thus, based on current Geant4 simulation, the relative accuracy on F_A is **39%**. Note that this is much larger than 12%, obtained in sec. VI without double-pion production contribution to the background. Additional optimization of the “wide veto” could improve the accuracy of the F_A measurement.

IX. DAQ TRIGGER LOGIC AND RATES

A. Overview

The experiment will use a 2.2 GeV beam of 120 μA on a 25 cm liquid hydrogen target. The target will be collimated using tungsten blocks to limit the visible region to the middle 10 cm. Neutrons will be detected in a solid angle given by $48 \pm 3.8^\circ$ (horizontal angle) $\times \pm 15^\circ$ (vertical angle). The second arm, the main veto, has sufficient solid angle for vetoing $e-p$ and π^+-n events.

In the two-body final state process, we can use a high energy threshold in the trigger. In case of neutron detection, the hadron calorimeter, NCAL, will be used. With 526 MeV neutron average kinetic energy in the $p(\bar{e}, n)\nu_e$ process, we plan to use a threshold corresponding to a 100 MeV combined energy deposition in the NCAL and TOF detectors. This will provide an acceptable rate and 60% detection efficiency for a Level-0 trigger. For our selected 3 MeV threshold on energy deposition in a single TOF counter, the combined efficiency of the full 11-layer TOF is about 25%. Due to the relatively low speed of the neutrons and large distance between the target and the time-of-flight counters, the propagation time for neutrons is 65.2 ns and for photons, 50 ns, so the photon induced hits can be removed at the trigger level. The veto arm will be used for high precision calibration of TOF and NCAL using elastic $e-p$ scattering at 2 μA beam current. During the main part of the run, the veto arm tracker (GEMs) will be switched OFF and the HCAL calorimeter signal will be used to veto the high energy electrons and pions (including secondary muons). The large energy of the pion/electron, 1.7 GeV, allows 98+% efficiency for HCAL for a 200 MeV threshold.

B. Online Level-0, Level-1 and Level-2 triggers

A Level-0 trigger will be formed by requiring a NCAL+TOF high energy hit (above 100 MeV). The projected rate of this trigger is 25 MHz (mostly photons).

A Level-1 trigger will be formed by requiring a time coincidence between the Level-0 trigger and a hit in TOF with a 0.25 m^2 geometric overlap between the TOF and NCAL hit locations in a 10 ns timing window, and exclude a narrow area of time in TOF relative to the beam bunch occupied by the prompt photons, which potentially contribute about 1.4 MHz rate. The projected rate of Level-1 is below 0.25 MHz.

A Level-2 trigger will require a tighter geometric correlation area of 15 cm x 15 cm, reducing the rate to 25 kHz, which is well within the capability of the proposed DAQ, see Appendix B in section XIII, and will allow us to record all HCAL, NCAL and TOF data.

The Level-1 and Level-2 triggers will be generated by a CPU in the front-end electronics.

C. Offline Analysis and Event Rate

A Level-3 event will require Level-2 but exclude events with large signals (>200 MeV) in the veto arm calorimeter HCAL. The projected rate of the Level-3 trigger is 2.5 kHz.

For Level-4 events, the NCAL energy and time resolutions will be updated (sigma 0.4 ns) and coordinate resolution also (sigma 4 cm). The same will be done for the TOF time resolution (sigma 125 ps) and coordinate resolution (sigma 1.5-2 cm). As a result, the updated cuts will lower the event rate to 300 Hz.

The final analysis will use the reconstructed beam energy with the cut from -16 to +16 MeV which will reduce the event rate to a few Hz, see also Sec. VI.

X. PREPARATION AND PLANS

This section presents our expectation on the timeline of the experiment preparation, cost of the project, and the collaboration commitments.

Following the release of the PAC52 report, which supports our LOI-12-24-009, we purchased four scintillator bars and the necessary PMTs for construction of counters similar to the ones developed in Ref. [56]. These counters will be used to study the time resolution using cosmic rays. Recently, thanks to H. Crawford, we found the components of the E864 calorimeter at BNL. The E864 calorimeter [57] has superior energy, time, and coordinate resolutions.

The JLab GlueX experiment has already collected data with 2 GeV photons on the LH2 target which could be analyzed for the neutron production rate. This will allow better estimate of the neutron energy spectrum related to the multi-pion reaction and check the Geant4 MC results.

Based on our experience with the SBS spectrometer project, we think that this experiment could be ready for installation in 5 years.

A. Timeline

After approval of the proposal by the JLab PAC, we plan to prepare a test run in Hall C with a prototype neutron detector that is 5% of the size of the planned neutron arm (without the sweeper magnet). We will use the HMS spectrometer as a veto arm and E864 blocks donated by BNL for the neutron arm and a “wide veto”. The goal of the test run will be to confirm our calculation of the time resolution and background rates. The following will be done in the test run:

- Test of the time-of-flight resolution for protons and neutrons.
- Measurement of the background production rate from Al, hydrogen, and deuterium.
- Test of the FPGA code for the online triggers.

Following the test run, we plan to prepare an MRE proposal to NSF, which will allow us to construct the TOF, NCAL and “wide veto”.

We are also exploring the possibility of using the large calorimeters of STAR (25 m²) and PHENIX for neutron detection. They could also be usable for the “wide veto” detector.

B. Anticipated Cost of the Neutron Arm

According to the list below, if most of components are new, the total cost is \$34.9M^{*}.

- Scintillator bars, 1540 x \$1.5k = \$2.3M
- PMTs (two per scintillator bar), 1540 x 2 x \$2k = \$6.2M
- Front-end discriminators, 3080 channels = \$0.6M
- NCAL 30 m², with 500 (from E864) + 2500 new modules, = \$18M^{*}
(estimate based on construction cost of Hall D and E684 calorimeters)
- The sweeper magnet and its power supply, = \$0.6M
- VME-based FADCs for each PMT in TOF and NCAL, 6080 channels = \$2.4M
- High resolution, 30 ps VETROC TDCs for TOF, 3080 channels = \$0.1M
- VXS crates, 2 for VETROCs + 23 for FADCs, = \$0.4M
- High voltage supply, 3600 channels (in addition to 2500 from ECAL/CDET from the GEP experiment) = \$1M
- Frames for the neutron arm detectors, = \$0.5M
- Tungsten for the collimator (about 50% is available from CPS project), = \$0.8M
- The “wide veto” calorimeter of 5 m² area with block’s design similar to HCAL, = \$2M^{*}

^{*} - Cost can be reduced by a factor of 2 if large BNL calorimeters can be used for NCAL and “wide veto”.

C. Workforce and Collaboration

Currently the AVFF collaboration is relatively small (74 persons). However, in view of the large interest in Axial-Vector Form Factor in the physics community, we anticipate that it will grow dramatically.

The current collaboration includes: Jefferson Lab, Temple University, William & Mary, Shandong University, INFN, UVa, AANL, Mississippi State University, and a number of other JLab users.

XI. SUMMARY AND BEAM REQUEST

We have two possible options to realize this experiment. The first one requires **55 days** of beam time and about **\$35M** capital funding for the detector construction. The second one needs twice as much beam time (**3.5 months**) but allows us to reach the same accuracy with twice smaller neutron arm acceptance and a reduced cost to about **\$20M**. We are looking for PAC advice on how to proceed, but focusing on the first option.

	Target	Beam energy, GeV	Beam, μA	Time, days
Calibration	LH2/LD2	2.2	1	2.5
Production	LH2	2.2	120	50
Beam polarization	Moller	2.2	1	2.5
Total requested time				55

TABLE III. The beam time plan in the AVFF experiment.

Here we are requesting **55 days of total beam time** to do a measurement of the proton Axial-Vector Form Factor at $Q^2 = 1$ $(\text{GeV}/c)^2$. Most of the time (50 days) will be used for statistics collection. We plan to do precision calibration of the time-of-flight system 10 times with 2.5 days included in total beam time. The calibration will include measurement of the detection efficiency of the neutron arm (TOF and NCAL) by using an LD2 target. We also plan to do five measurements of the beam polarization, which also require 2.5 days included in the request.

This experiment will take place in Hall C or Hall A, utilizing a 120 μA 2.2 GeV electron beam with a high degree of longitudinal polarization. Neutrons will be detected using a TOF system plus a hadron calorimeter preceded by a sweeper magnet to eliminate most of the charged particle background. A veto arm detector will be designed to reject events from the two largest background processes: $e-p$ elastic electron scattering and pion photo-production.

The experimental result will be the cross section value of the reaction $p(\vec{e}, n)\nu_e$ at $Q^2 = 1$ $(\text{GeV}/c)^2$. The cross section varies close to linearly with F_A , so the relative accuracy for the Axial-Vector Form Factor is the same as for the cross section, and the projected relative accuracy of F_A **will be 39%** (statistical) with systematics of 5%.

LOI12-24-009

Title: Measurement of the Nucleon Axial Vector Form Factor at $Q^2 = 1 \text{ (GeV/c)}^2$

Spokespersons: B. Wojtsekhowski (contact)

Motivation: This LOI proposes to measure the axial-vector form factor of the nucleon using the reaction $H(e^-, n)\nu_e$. Most of the existing experimental measurements of this form factor come from neutrino scattering experiments with wide-band beams and often with nuclear targets. In contrast, the uniqueness of the proposed measurement is that it will use a mono-chromatic (known) beam and a nucleon target. Knowledge of the axial-vector form factor is becoming increasingly important for precision accelerator-based neutrino oscillation experiments, especially for those that compare neutrinos and antineutrinos.

Measurement and Feasibility: The request is for 25 days of electron data-taking at 2.2 GeV on a liquid hydrogen target in Hall C. For the detector, the proposal is to use the electron/pion arm from the existing SBS magnet, the SBS GEM chambers, and the lead-glass electromagnetic calorimeter that is currently under construction for the Gep experiment E12-07-109, which will run in 2025. The rest of the experimental needs will require new investment.

Given that the neutrino signal being probed is ~ 7 -8 orders of magnitude smaller than the elastic electron scattering and pion photo-production reactions, the proposed measurement requires significant strategies for background rejection ($\sim x 10^4$ rejection for the e-p process). While the precision of the measurement will depend strongly on the success of such background rejection, even an initial measurement of $G_A(Q^2)$ at twice the quoted precision would be valuable, given the dearth of existing experimental data.

Issues: The LOI is short on detail and lacking in physics plots. Overall, the proposal needs a more detailed description of the measurement itself, the associated theory, and the detector setup that will be used. A full simulation and description detailing the strategy for background rejection will be critical content for a full proposal. A plot of the planned accuracy of the axial-form factor measurement compared to existing measurements should be produced. It will also be important to tabulate to what extent existing vs. new experimental equipment will be required to carry out the planned measurement.

Summary: This LOI offers a unique opportunity to measure the axial-vector form factor (the least well-known nucleon form factor) in a very different manner than is commonly probed in neutrino scattering. Such a measurement is of considerable importance for accelerator-based neutrino oscillation experiments. The PAC encourages the proponents to proceed to a full proposal after the above issues are addressed. The PAC encourages the use of a full Monte Carlo simulation to assess detector performance, background levels, and systematic uncertainties. If this method of extracting the axial-vector form factor proves successful, the PAC notes that this could become part of a larger measurement campaign. In particular, a measurement of the Q^2 dependence of the axial-vector form factor would be of great interest to the neutrino scattering community.

In addition to the LOI12-24-009, we note that three other LOIs with the aim to measure F_A based on polarized electron or positron beam had been submitted to Jefferson Lab PAC over 37 years [6, 7, 27].

XIII. APPENDICES

A. Wide-angle Compton Scattering

P. Kroll, *Fachbereich Physik, Universität Wuppertal, D-42097 Wuppertal, Germany*

For Compton scattering there are two kinematical regions in which QCD factorization properties allows us to calculate Compton scattering. On the one hand, this is the region of large photon virtualities, Q^2 and large energies in the photon-proton center-of-mass system but small Mandelstam $-t$ ($-t \ll Q^2$). It has been shown [20, 62] that in this region the Compton amplitudes are represented as a convolution of a hard partonic subprocess and soft hadronic matrix elements parameterized as generalized parton distributions (GPDs). The other kinematical region in which factorization applies [34, 63] is the wide-angle region, i.e. the region where all Mandelstam variables, s , $-t$ and $-u$, are large. It has been argued [63] that in a zero-skewness frame and provided that the three Mandelstam variables are much larger than a typical hadronic scale, Λ^2 , of $1(\text{GeV}/c)^2$, the Compton amplitudes factorize in a product of hard subprocess amplitudes and form factors which represent $1/x$ -moments of zero-skewness GPDs.

It is of advantage to work in a symmetric frame where the momenta of the initial (p) and final (p') state protons are parameterized as

$$p^{(\prime)} = \left[p^+, \frac{m^2 - \Delta_\perp^2/4}{2p^+}, \frac{-1}{(+)} \frac{\Delta_\perp}{2} \right] \quad (35)$$

in light-cone coordinates. The photon momenta (q and q') are defined analogously. Obviously, in this frame $t = \Delta_\perp^2$ and the skewness, $\xi = (p - p')^+ / (p + p')^+$, is zero. In [63] it is assumed that the parton virtualities are restricted by $k_i^2 < \Lambda^2$ and that the intrinsic transverse momenta, $k_{\perp i}$, defined with respect to their parent hadron's momentum, satisfy the condition $k_{\perp i}^2/x_i < \Lambda^2$ where $x_i = k_i^+ / p^+$ is the momentum fraction that parton i carries. One can then show that, up to corrections of order $\Lambda/\sqrt{-t}$, the subprocess Mandelstam variables, $\hat{s}, \hat{t}, \hat{u}$, coincide with the ones for the full process

$$\hat{t} = t, \quad \hat{s} = (k_j + q)^2 \simeq (p + q)^2 = s, \quad \hat{u} = (k'_j - q)^2 \simeq (p' - q)^2 = u, \quad (36)$$

where k_j and $k'_j = k_j + q - q'$ denote the momenta of the active partons, i.e. those partons to which the photon couple. Hence, the active partons are approximately on-shell, move collinear with their parent hadrons and carry a momentum fraction close to unity, $x_j, x'_j \simeq 1$. As in deeply virtual Compton scattering, the physical situation is that of a hard parton-level subprocess, Compton scattering off quarks, and a soft emission and reabsorption of quarks from the baryons. Thus, up to corrections of order $\Lambda/\sqrt{-t}$, one can write the (light-cone) helicity amplitude for wide-angle Compton scattering (WACS) as [22, 63]

$$\begin{aligned} \mathcal{M}_{\mu'+, \mu+}(s, t) &= 2\pi\alpha_{\text{em}} \left[\mathcal{H}_{\mu'+, \mu+}(\hat{s}, \hat{t})(R_V(t) + R_A(t)) \right. \\ &\quad \left. + \mathcal{H}_{\mu'-, \mu-}(\hat{s}, \hat{t})(R_V(t) - R_A(t)) \right], \\ \mathcal{M}_{\mu'-, \mu+}(s, t) &= \pi\alpha_{\text{em}} \frac{\sqrt{-t}}{m} \left[\mathcal{H}_{\mu'+, \mu+}(\hat{s}, \hat{t}) + \mathcal{H}_{\mu'+, \mu+}(\hat{s}, \hat{t}) \right] R_T(t). \end{aligned} \quad (37)$$

The non-zero LO amplitudes, $\mathcal{H}_{\mu'\lambda', \mu\lambda}$ for the subprocess $\gamma(\mu)q(\lambda) \rightarrow \gamma'(\mu')q'(\lambda')$ where the symbols in the brackets denote the helicities, read

$$\mathcal{H}_{+,+,++} = 2\sqrt{\frac{\hat{s}}{-\hat{u}}}, \quad \mathcal{H}_{+,-,+} = 2\sqrt{\frac{-\hat{u}}{\hat{s}}}. \quad (38)$$

NLO corrections have also been calculated [22]. The form factors are given by the sum

$$R_i(t) = \sum_a e_a^2 R_i^a(t) \quad (39)$$

where a is the flavor of the active quark and e_a the quark charge. The flavor form factors read

$$R_{V(T)}(t) = \int_{-1}^1 \frac{dx}{x} H^a(E^a)(x, t), \quad R_A(t) = \int_{-1}^1 \frac{dx}{x} \text{sign}(x) \tilde{H}^a(x, t). \quad (40)$$

The Compton cross section is given by

$$\frac{d\sigma}{dt} = \frac{\pi\alpha_{\text{em}}^2}{(s-m^2)^2} \frac{(s-u)^2}{-us} \left[R_V^2 + \frac{t^2}{(s-u)^2} R_A^2 - \frac{t}{4m^2} R_T^2 \right]. \quad (41)$$

There is also a number of spin effects. Particularly interesting for our purpose are the correlations between the helicities of the incoming photon and the incoming (A_{LL}) or outgoing (K_{LL}) proton. These correlations are approximately given by [29]

$$A_{LL} = K_{LL} \simeq 2 \frac{-t}{s-u} \frac{R_A^\gamma(t)}{R_V^\gamma(t)}. \quad (42)$$

In [3, 64] the nucleon form factors have been analyzed in terms of zero-skewness GPDs. The following parameterization of the GPDs, K_i , has been advocated for in these papers

$$K_{iv}^a(x, t) = k_i^a(x) \exp [t f_i^a(x)] \quad (43)$$

with the profile function

$$f_i^a(x) = (\alpha_i^a \ln(1/x) + B_i^a)(1-x)^3 + A_i^a x(1-x)^2. \quad (44)$$

The forward limits of the GPDs, $k_i^a(x)$, are given by the polarized and unpolarized parton distributions for \tilde{H} and H , respectively. For E it is parameterized analogously to the parton distributions with a number of additional free parameters to be adjusted to the form factor data. An important property of the parameterization (43), (44) is the strong $x-t$ correlation: large (small) x go together with large (small) $-t$. This implies that at large $-t$ the moments of the GPDs are dominated by valence quarks; the sea-quark contribution is negligible since the sea-quark distributions vanish with higher power, β_i , of $1-x$ for $x \rightarrow 1$ than the valence quarks. It has also been shown in [63] that (43) leads to a power-law behavior of the nucleon form factors at sufficiently large $-t$ where the power is $(1 + \beta_i)/2$. This is to be contrasted with the frequently used Regge-like parameterization of the GPDs (i.e. $A_i = 0$ and the factor $(1-x)^3$ omitted in (44)) which leads to exponentially falling form factors.

In [3] the valence-quark GPDs H and E have been rather well determined from the data on the electric and magnetic nucleon form factors and subsequently the Compton form factors R_V and R_T . It turned out that $R_T(t) \ll R_V(t)$. The axial form factor, on the other hand, is not well fixed in [3]. Because of the lack on the axial form factor, F_A , \tilde{H} has been approximated in [3] by the profile function of H multiplied with the polarized parton distribution. Evaluation of the Compton form factor R_A from this GPD leads to a result that is somewhat smaller than R_V ; at $t \simeq 10$ (GeV/c)² R_A amounts to about 80% of R_V . The WACS cross section evaluated from these Compton form factors agrees fairly well with experiment (see [3]). For spin-dependent observables, measured at rather small values of s , the agreement with experiment is less good. This may be owed to the rather small values of s at which these observables have been measured and/or to the badly known GPD \tilde{H} at large $-t$ or the Compton form factor R_A . New data on R_A at large $-t$ could improve the situation.

Another application of GPDs at large $-t$ and where data on F_A would be helpful is the study of parton localization in the impact parameter plane. As shown by Burkardt [65] a density interpretation of zero-skewness GPDs is obtained in the mixed representation of longitudinal momentum and transverse position in the infinite momentum frame. In particular,

$$q_{\pm}^a(x, b^2) = \frac{1}{2} \int \frac{d^2 \Delta_{\perp}}{4\pi^2} e^{-i\mathbf{b} \cdot \mathbf{\Delta}_{\perp}} \left[H^a(x, 0, t = -\Delta_{\perp}^2) \pm \tilde{H}^a(x, 0, t = -\Delta_{\perp}^2) \right] \quad (45)$$

is the impact-parameter distribution of flavor- a quarks with helicity parallel (+) or antiparallel (-) to the proton's helicity. In (45) $\mathbf{\Delta}_{\perp}$ is the momentum transfer from the initial to the final proton. Obviously, for a reliable Fourier transform the GPDs H and \tilde{H} are required at fairly large $-t$. In the figure the impact-parameter distribution for valence quarks with definite helicities are shown. The distributions have been evaluated from a recent parameterization of the valence-quark GPDs [4]. A possible sea quark contribution is ignored. One observes from the figure the typical behavior of the impact-parameter distributions: a very broad distribution at low x which becomes narrower with increasing x , i.e. for $x \rightarrow 1$ the active parton is close to the proton's center of momentum. Another feature is the dominance of u -quarks with the same helicity as the proton at large x . This behavior is expected from perturbative QCD for $x \rightarrow 1$ [66]. The behavior of the d -quark distribution is not in agreement with the perturbative QCD predictions, at least not at $x = 0.6$.

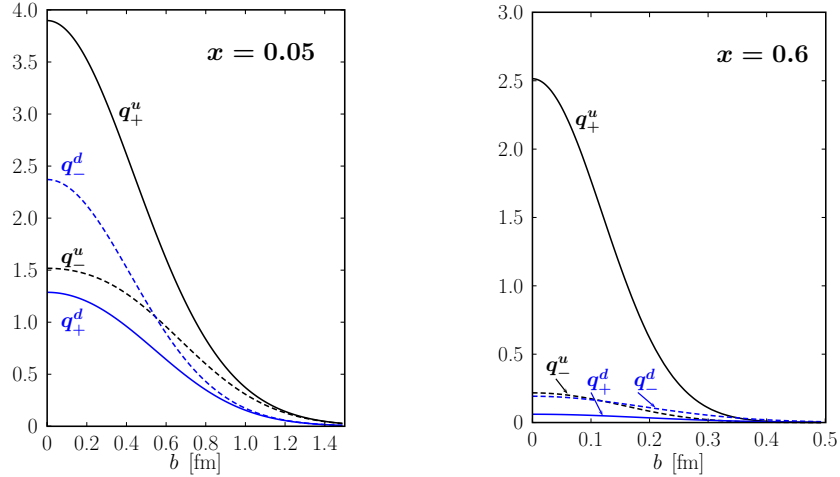


FIG. 31. The impact-parameter distributions of valence quarks with definite helicities (in fm^{-2}) at $x = 0.05$ (left) and 0.6 (right). The figure is taken from [4].

B. Data acquisition system

B. Raydo, *Jefferson Lab, Fast Electronics and Data Acquisition Group*

The DAQ system will use standard JLab configured VXS crates, shown in Fig. 32. The NCAL analog signals will be digitized with the FADC250 shown in Fig. 33-Left. The TOF signals, in addition to FADC250, will be sent to the high resolution TDC VETROC [67] or V1290N-2eSST produced by CAEN [68]. Details are given in Table IV

TDC specs (V1190A/VX1290A)		FADC250 specs	
No. Channels	128/32	No. Channels	16
RMS resolution	100 ps/25 ps	Sampling	250 MHz
Resolution	19 bit/21 bit	Resolution	12-bit
Inter-channel isolation	≤ 3 LSB	Clock jitter	350 fs
Double-hit resolution	5 ns	Data Memory	8 μ s
Full-scale range	52 μ s	Trigger/Data latency	8 μ s / 32 ns
Inter-channel isolation	< 3 LSB	SNR	56.8 dB @ 100 MHz input
Integral/Differential non-linearity:			
2.5 LSB / < 3 LSB		± 0.5 LSB / ± 0.8 LSB	

TABLE IV. Specifications for the TDC and FADC modules planned for this experiment. Data taken from [56].

Data from the FADC250 and TDC modules are streamed to the VTP (Fig. 35) where filtering is done on the NCAL data to reduce the data rate before NCAL and TOF data are streamed out using up to four 10 Gbps Ethernet links, from each readout crate, to the servers for storage. The behavior of these modules and processing procedures are described in the following sections.

1. VXS Crate

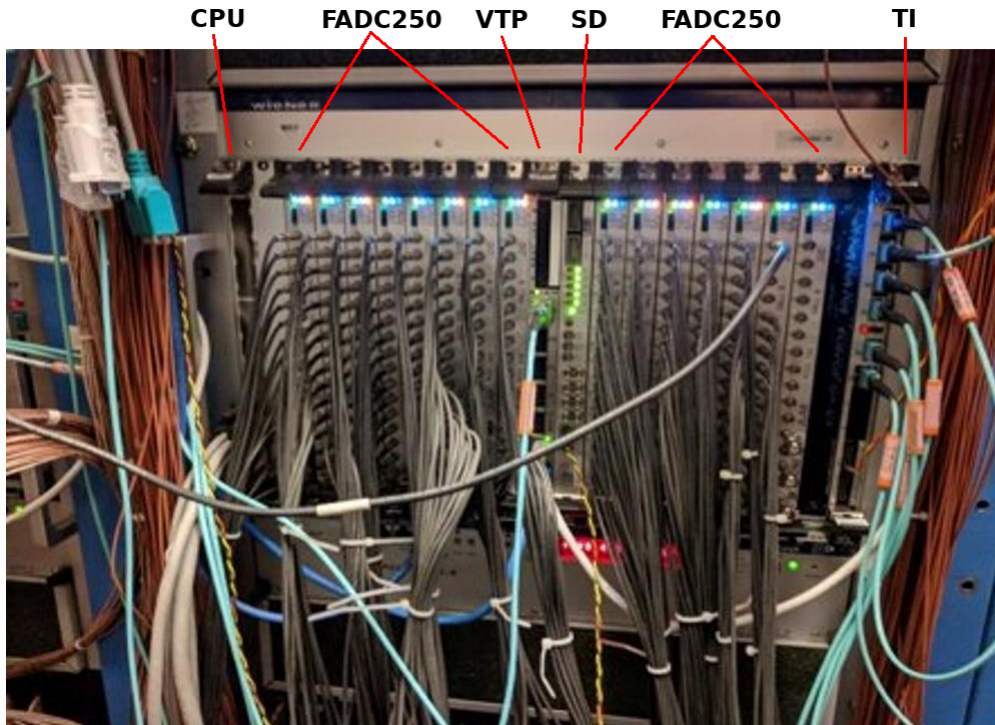


FIG. 32. JLab VXS Crate of FADC250 modules. CPU is used for configuration, VTP for trigger processing and readout, SD to distribute DAQ synchronization signals, TI to receive DAQ synchronization signals from global trigger system.

A 21-slot VXS crate supports up to 16 front-end modules (e.g. 16 FADC250 modules for 256 FADC channels, 16 V1290N-2eSST modules, or a mixture of these modules). A CPU is used to configure, monitor, and (optionally) readout front-end modules. The TI and SD modules are responsible for receiving and distributing the global DAQ clock, trigger, and sync signals to all front-end modules so that all front-end modules in the full system (across multiple crates) remain synchronized. The system clock jitter is under 10 ps RMS, contributing negligibly to the timing noise typically achievable by the pulses captured by the FADC250 and TDC modules used at JLab. A VTP communicates with each front-end module with bidirectional high speed serial links (10 Gbps to 20 Gbps per module), processes data, and streams data out over up to 4 of its 10 Gbps optical Ethernet ports. The CPU readout speed is limited by VME (200 MB/s in total from all front-ends) and 1 Gbps Ethernet ports to roughly 120 MB/s. The VTP readout speed is limited by VXS (200MB/s per front-end) and one to four 10 Gbps Ethernet ports which each can transport 1 GB/s.

2. JLab FADC250

The FADC250 is a VME/VXS 16 channel flash analog-to-digital converter module used in many experimental setups at JLab.



FIG. 33. Left: FADC250 - JLab 16 channel VME/VXS based 250MSPS Flash ADC digitizer. Right: VETROC - JLab 128 channel TDC. Expansion/rear transition card that supports an additional 64 TDC channels is shown.

It continuously samples the analog inputs at 250 MHz and stores all raw samples in a $8 \mu\text{s}$ ring buffer, waiting for trigger decisions to choose what to read out. It also detects, integrates, and sends individual pulse charge integrals and timestamps to the VTP over the VXS backplane for readout and/or triggering purposes. This pulse processing on the FADC250 can be seen in Fig. 34.

3. JLab VTP

The VTP is a switch style VXS board that is connected to all front-end cards over the VXS back using 4 bidirectional serial links that can run up to 8 Gbps each. Normally these links run at 3.125 Gbps or 5 Gbps depending on the application, providing from 12.5 Gbps to 20 Gbps bandwidth between each front-end and the VTP. These links are used to stream hits and control information for readout and/or triggering purposes. A XC7V550T FPGA is used to collect the serial streaming, buffer data, and process data. A XC7Z7030T FPGA collects the final readout stream from the XC7V550T and can send it over any of the four 10 Gbps Ethernet optical links using UDP and/or TCP to commercial computers.

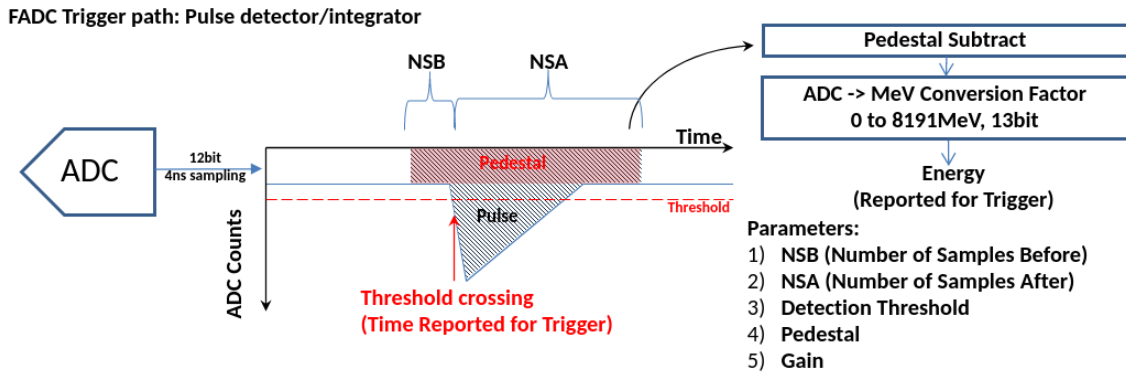


FIG. 34. FADC250 pulse detection, integration, reporting.

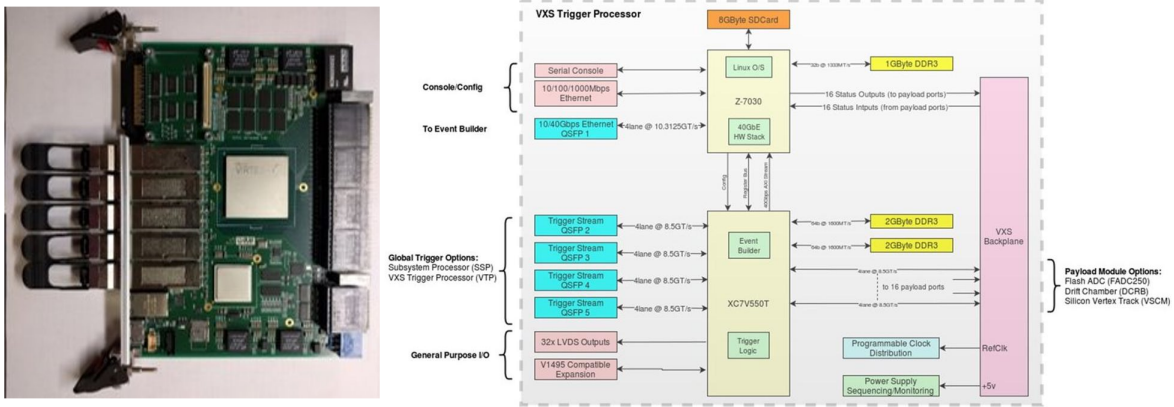


FIG. 35. VTP (VXS Trigger Processor) Module.

4. Streaming and Filtering logic

The VTP receives all FADC250 detected pulses (integrals and 4 ns resolution timestamps) and performs clustering in space and time looking at all 3x3 crystal views in HyCal. The NCal requires more FADC250 channels than can fit within a single VXS crate - 5 VXS crates and VTPs are needed for HyCal. The VTP shares FADC250 hits along these borders with adjacent crate VTPs so that each VTP can perform 3x3 clustering without missing channels due to the border. This is accomplished using the VTP optical links - there are 4 of them and each can exchange 32 channels over the link.

Hits in the 3x3 cluster view that are within the programmable timing coincidence window are summed and this result is checked against a programmable threshold. The 3x3 clustering is illustrated in the example shown in Fig. 36. When a cluster is found to be over threshold, the VTP sends a fixed latency command back to the FADC250 telling them to report the pulse integrals (without gain or pedestal subtraction applied) for a 5x5 group of channels centered on the initial 3x3 cluster. The

e.g. for seed threshold of 2 and hit $\Delta t = \pm 8$ ns, the following hit pattern evolving in time will report 1 cluster:

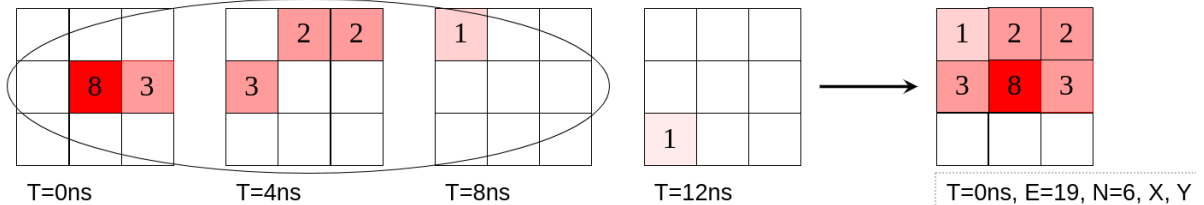


FIG. 36. 3x3 clustering used in filtering.

VTP collects these 5x5 groups view of pulse integrals and packages this data in a compact form of 25 16-bit values (representing the pulse integrals of all channels in the 5x5 cluster), an 11-bit cluster coordinate, and a 48-bit 4-ns resolution timestamp. This 58-byte packaged cluster data is sent from each VTP with an overall expected cluster rate of 20 MHz resulting in a HyCal cluster data rate of 1.1 GByte/sec, which comfortably fits in the five (up to 20 links available) 10 Gbps Ethernet links used to stream from the VTP (if needed, an additional two 10 Gbps Ethernet links from each VTP are also available). One of the 10 Gbps Ethernet links from each VTP will be used to stream unfiltered VETROC hits from the MWPC.

5. DAQ Crate System Layout

The NCAL crates require special segmentation to allow the system to perform clustering across crate boundaries. The NCAL crate setup is shown in Fig. 37. HyCal is segmented into 5 sections which allow the VTP to be able to exchange FADC hits near the crate boundaries to adjacent VTPs so clustering can be accomplished correctly. Additionally, these optical links will be used to provide the final streamed FADC pulse integrals of clusters to be exchanged so that VTPs can also build a complete cluster event. There are 4 optical links per VTP, which typically run at 20 Gbps, but are scalable to 34 Gbps. The FADC hit shared for clustering requires 34 channels of 16 bits at 31.25 MHz to be exchanged, resulting in 21.25 Gbps utilization (with 8b10b encoding overhead). This requires 2 optical links to be used, which is no problem. The remaining 18.75 Gbps is available for exchanging the final cluster pulse integrals and control information, which is also no problem, for a **total of 20 MHz cluster readout rate**.

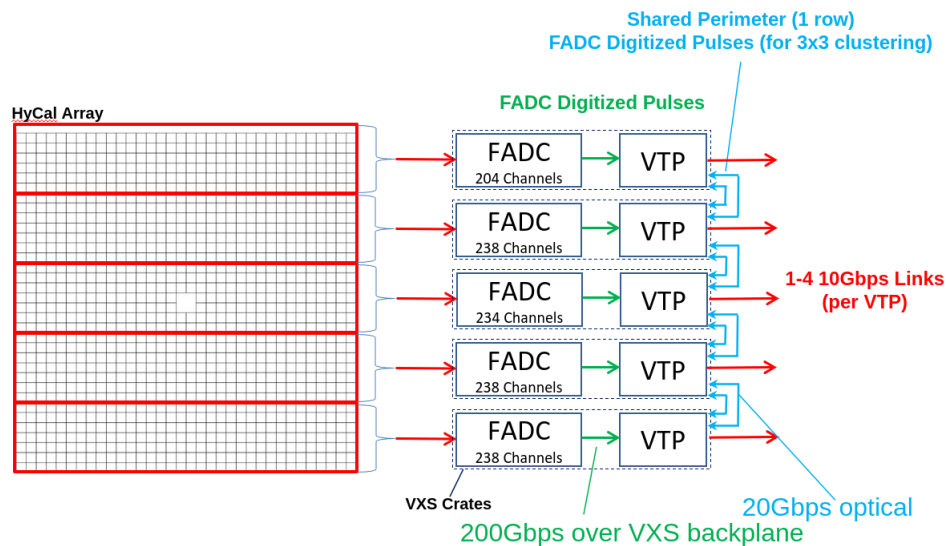


FIG. 37. HyCal DAQ Crate Layout.

The resulting hit rate limits are 250 MHz per 10 Gbps Ethernet used by the VTP streaming output (up to 1 GHz hit readout rate using all 4 Ethernet links from the VTP).

The VTP has been used for streaming readout in JLab experiments since 2020, and the DAQ group has implemented support for this system in the CODA framework. Several small scale experiments have used the VTP streaming system, the CLAS12 Forward Tagger Calorimeter and Hodoscope being the first, see Refs. [69, 70].

6. Conclusion

The dominating data source is the NCAL/TOF/HCAL streaming FADC hits, but with the hit stream filtering we expect no more than 3 MHz of clusters in the energy region of interest. The compact data packing of 58 bytes for the upper limit of 3 MHz of clusters, 0.2 GB/s, is well under the VTP streaming readout bandwidth (1 GB/s planned, with 20 GB/s capacity if ever needed).

-
- [1] A. S. Meyer, A. Walker-Loud, and C. Wilkinson, *Ann. Rev. Nucl. Part. Sci.* **72**, 205 (2022), arXiv:2201.01839 [hep-lat].
- [2] C. Alexandrou *et al.*, *Phys. Rev. D* **103**, 034509 (2021), arXiv:2011.13342 [hep-lat].
- [3] M. Diehl and P. Kroll, *Eur. Phys. J. C* **73**, 2397 (2013), arXiv:1302.4604 [hep-ph].
- [4] P. Kroll, *Eur. Phys. J. A* **53**, 130 (2017).
- [5] T. Cai *et al.* (MINERvA), *Nature* **614**, 48 (2023).
- [6] J. Napolitano, Measurement of the Nucleon Weak Axial Vector Form Factor (1988), Letter of Intent to JLab PAC1.
- [7] A. Deur, Measurement of the Q^2 dependence of the axial-vector and pseudoscalar nucleon form factors from $Q^2 = 1$ to 3 $(\text{GeV}/c)^2$ (2003), Letter of Intent 04-006 to JLab PAC25.
- [8] J. Napolitano and B. Wojtsekhowski, Measurement of the Nucleon Axial Vector Form Factor at $Q^2 = 1$ $(\text{GeV}/c)^2$ (2024), Letter of Intent 12-24-009 to JLab PAC52.
- [9] Y. Nambu and E. Shrauner, *Phys. Rev.* **128**, 862 (1962).
- [10] Y. Yu.I. Titov *et al.*, *Physics Letters B* **37**, 422 (1971).
- [11] V. Bernard, L. Elouadrhiri, and U.-G. Meissner, *J. Phys. G: Nucl. Part. Phys.* **28** (2002).
- [12] A. S. Meyer *et al.*, *Phys. Rev. D* **93**, 113015 (2016).
- [13] NSAC, A new era of discovery. The 2023 long range plan for nuclear science (2023).
- [14] C. A. Argüelles *et al.*, Snowmass white paper: beyond the standard model effects on neutrino flavor (2023).
- [15] R. Alarcon *et al.*, Fundamental neutron physics: a white paper on progress and prospects in the us (2023), arXiv:2308.09059 [nucl-ex].
- [16] O. Benhar, P. Huber, C. Mariani, and D. Meloni, *Physics Reports* **700**, 1 (2017).
- [17] L. Jiang *et al.*, *Phys. Rev. D* **105**, 112002 (2022).
- [18] L. Jiang *et al.*, *Phys. Rev. D* **107**, 012005 (2023).
- [19] D. Müller *et al.*, *Fortschritte der Physik* **42**, 101 (1994).
- [20] X.-D. Ji, *Phys. Rev. D* **55**, 7114 (1997), arXiv:hep-ph/9609381.
- [21] A. Radyushkin, *Physics Letters B* **380**, 417 (1996).
- [22] H. W. Huang, P. Kroll, and T. Morii, *Eur. Phys. J. C* **23**, 301 (2002), [Erratum: *Eur.Phys.J.C* 31, 279 (2003)], arXiv:hep-ph/0110208.
- [23] D. Hamilton, V. Mamyan, *et al.* (Jefferson Lab Hall A Collaboration), *Phys. Rev. Lett.* **94**, 242001 (2005).
- [24] C. Chen and C. D. Roberts, *The European Physical Journal A* **58**, 206 (2022).
- [25] PAC5, JLab PAC5 report on G0 experiment (1992).
- [26] D. Armstrong *et al.* (G0), *Phys. Rev. Lett.* **95**, 092001 (2005), arXiv:nucl-ex/0506021.
- [27] D. Dutta, The Axial Form Factor of the Nucleon from Weak Capture of Positrons (2023), Letter of Intent to JLab PAC51.
- [28] Z. Ye, J. Arrington, R. J. Hill, and G. Lee, *Phys. Lett. B* **777**, 8 (2018), arXiv:1707.09063 [nucl-ex].
- [29] P. Kroll, Technical note for the AVFF proposal (2024).
- [30] C. H. Llewellyn Smith, *Phys. Rept.* **3**, 261 (1972).
- [31] B. Wojtsekhowski *et al.*, Jefferson Lab PAC 16 Proposal: Exclusive Compton Scattering from the Proton (1999).
- [32] A. Danagoulian, V. Mamyan, *et al.* (Jefferson Lab Hall A Collaboration), *Phys. Rev. Lett.* **98**, 152001 (2007).
- [33] C. Fanelli *et al.*, *Phys. Rev. Lett.* **115**, 152001 (2015).
- [34] A. V. Radyushkin, *Phys. Rev. D* **58**, 114008 (1998), arXiv:hep-ph/9803316.
- [35] G. D. Megias, S. Bolognesi, M. B. Barbaro, and E. Tomasi-Gustafsson, *Phys. Rev. C* **101**, 025501 (2020).
- [36] P. Adamson *et al.*, *Nucl. Instrum. Meth. A* **806**, 279 (2016), arXiv:1507.06690 [physics.acc-ph].
- [37] B. G. Tice *et al.* (MINERvA Collaboration), *Phys. Rev. Lett.* **112**, 231801 (2014).
- [38] C. Andreopoulos *et al.*, *Nucl. Instrum. Meth. A* **614**, 87 (2010), arXiv:0905.2517 [hep-ph].
- [39] S. Navas and others. (Particle Data Group Collaboration), *Phys. Rev. D* **110**, 030001 (2024).
- [40] G. Bali *et al.*, *Journal of High Energy Physics* **2020**, 126 (2020).
- [41] T. Hague *et al.*, Updated analysis of neutron magnetic form factor and the nucleon transverse densities (2025).
- [42] R. L. Anderson *et al.*, *Phys. Rev. D* **14**, 679 (1976).
- [43] D. G. Meekins *et al.*, *Phys. Rev. C* **60**, 052201 (1999).
- [44] J. Napolitano *et al.*, *Phys. Rev. Lett.* **61**, 2530 (1988).
- [45] E. C. Schulte *et al.*, *Phys. Rev. C* **66**, 042201 (2002).
- [46] I. A. Qattan *et al.*, High precision measurements of the proton elastic electromagnetic form factors and their ratio at $q^2 = 0.50, 2.64, 3.20, \text{ and } 4.10 \text{ geV}^2$ (2024), arXiv:2411.05201 [nucl-ex].
- [47] J. J. Kelly, *Phys. Rev. C* **70**, 068202 (2004).
- [48] W. R. Gibbs and B. Loiseau, *Phys. Rev. C* **50**, 2742 (1994).
- [49] W. Hürster and others, *Physics Letters B* **90**, 367 (1980).
- [50] O. Benhar *et al.*, *Nuclear Physics A* **579**, 493 (1994).
- [51] V. M. Budnev, I. F. Ginzburg, G. V. Meledin, and V. G. Serbo, *Phys. Rept.* **15**, 181 (1975).
- [52] M. Dugger *et al.* (CLAS), *Phys. Rev. C* **79**, 065206 (2009), arXiv:0903.1110 [hep-ex].
- [53] SAID, The SAID Partial-Wave Analysis Facility (2025).
- [54] O. Benhar, D. Day, and I. Sick, *Rev. Mod. Phys.* **80**, 189 (2008).
- [55] E. Schulte, $\text{Al}(\gamma, p)$ cross section (2025), private communication.

- [56] D. Carman *et al.*, Nuclear Instruments and Methods in Physics Research Section A: Accelerators, Spectrometers, Detectors and Associated Equipment **960**, 163629 (2020).
- [57] T. Armstrong *et al.*, Nuclear Instruments and Methods in Physics Research Section A: Accelerators, Spectrometers, Detectors and Associated Equipment **406**, 227 (1998).
- [58] S. Jeffas, *Measurement of the Neutron Electromagnetic Form Factor Ratio at High Momentum Transfer*, Phd thesis, UVA (2024), https://libraetd.lib.virginia.edu/public_view/xg94hr23t.
- [59] S. Seeds, *The Two-Photon Exchange Contribution to Electron-Neutron Elastic Scattering ...*, Phd thesis, UConn (2024), https://puckett-physics.media.uconn.edu/wp-content/uploads/sites/1958/2024/09/SebastianSeedsThesisAugust2_2024.pdf.
- [60] R. Suleiman, Injector parameters (2025), JLab technical note.
- [61] S. Zhang, Status of the cebaif photo-injector drive laser system for klong beam (2023).
- [62] J. Collins, L. Frankfurt, and M. Strikman, Phys. Rev. D **56**, 2982 (1997), arXiv:hep-ph/9611433.
- [63] M. Diehl, T. Feldmann, R. Jakob, and P. Kroll, Eur. Phys. J. C **8**, 409 (1999), arXiv:hep-ph/9811253.
- [64] M. Diehl, T. Feldmann, R. Jakob, and P. Kroll, Eur. Phys. J. C **39**, 1 (2005), arXiv:hep-ph/0408173.
- [65] M. Burkardt, Int. J. Mod. Phys. A **18**, 173 (2003), arXiv:hep-ph/0207047.
- [66] S. J. Brodsky, M. Burkardt, and I. Schmidt, Nucl. Phys. B **441**, 197 (1995), arXiv:hep-ph/9401328.
- [67] S. Boyarinov, B. Raydo, and W. Gu, CLAS12 DAQ upgrade plan (2020), report.
- [68] CAEN, High resolution TDC V1290N-2eSST (2025), CEAN web page.
- [69] F. Ameli *et al.*, (2021).
- [70] M. Bondi, Streaming data acquisition system for clas12 forward tagger (2021).